Chapter 2: The Mars Exploration Rover and the Athena Science Payload

2.1 The Mars Exploration Rover (MER)

Spirit and Opportunity are "twin" rovers, launched from Earth in the early summer of 2003. They arrived on opposite sides of Mars in January 2004, on a mission to "explore two sites on the Martian surface where water may once have been present, and to assess past environmental conditions at those sites and their suitability for life" [*Squyres et al.* 2003]. Each rover was required to be capable of [*Crisp et al.* 2003]:

1) Returning 2 color stereo Pancam and 2 Mini-TES panoramas.
2) Driving to at least 4 distinct locations and performing in situ measurements at each location.
3) Returning measurements using the full instrument suite of at least 1 soil sample, 4 rocks, and 1 abraded rock.
4) Driving at least 600m.
5) Lasting for 90 sols with full use of the complete instrument suite.
6) Performing one soil mechanics experiment and returning the associated measurements necessary for characterizing soil physical properties.
7) Returning the supporting calibration measurements, imaging and Mini-TES measurements that enable characterization of the context and diversity of the landing sites.

They exceeded these goals, by far. As of May 16th, 2015 Opportunity has travelled over 42.26 km and survived for 4020 sols[1]. The team lost contact with Spirit on March 22nd, 2010, as she entered her fourth martian winter. Despite a complex and extensive campaign to contact the rover throughout the following spring, she was declared lost on May 25th, 2011 [*John Callas* 2011, personal communication]. She drove 7.7305 km during her 2210-sol lifetime.

---

[1] A Sol is a martian day, which is 24 hours, 37minutes, and 22.66 seconds [*Murry and Dermott*, 1999].

2.1.1 Rover dimensions

The rovers were designed to be robotic field geologists, and equipped with a payload (see Figure 4, and descriptions below) intended to enable the Mars Exploration Rover Team to examine the geology and geologic history of their field sites: Gusev Crater (Spirit) and Meridiani Planum (Opportunity). The Gusev landing site is described in Chapter 4. Unlike their predecessor, the Sojourner microrover [*Rover Team* 1997], the MERs are relatively humanlike in scale (see Table 1).

Table 1. Physical characteristics of the Mars Exploration Rovers. Values are from *Crisp et al.* [2003].

Rover Characteristic	Value
Mass	180 kg
Height	154 cm
Width at wheelbase	122 cm
Length at wheelbase	141 cm
Width at solar panels	225 cm
Length at solar panels	151 cm
Wheel diameter	26 cm
Turning diameter (turning in place)	1.9 m
Turning diameter (skid steering)	0.9 m
Top speed	4 cm/s

2.1.2 Mobility

The rover has six wheels, each 26cm in diameter. All are independently actuated, and four can be steered; the rover can rotate in place with a turning diameter of 1.9 m [*Crisp et al.* 2003]. A rocker-bogey suspension system, similar to those on the Mars Pathfinder Sojourner and Mars Science Laboratory Curiosity rovers, enables the rover to navigate uneven ground, and drive over obstacles up to approximately the size of its wheels (26cm) [*Crisp et al.* 2003]. The rover is capable of autonomous navigation, using its Navcam and Hazcam systems, towards a target selected by the rover team [*Crisp et al.* 2003, *Maki et al.* 2003].

2.1.3 Power

The rover generates power through solar cells on the rover deck and fold-out panels (see Figure 4) that were deployed after landing, and can store energy in two 8 A-hour Li-ion rechargeable batteries [*Crisp et al.* 2003]. The solar panels generated about 900 W-hours per sol at the start of the mission. Power generation slowly decreased as dust accumulated upon the cells, and increased when wind events removed dust from the rover. Opportunity experiences relatively frequent, gentle cleaning events. Spirit experienced fewer events, but they substantially cleaned the panels: the Sols 419-420 event doubled the rover's power [*Arvidson et al.* 2006], which enabled the team to command the rover to spend Sols ~460-510 examining Cumberland Ridge rather than focusing on finding "lilypads"[2] of north-facing slopes on a traverse across Husband Hill.

2.1.4 Pancam Mast Assembly (PMA)

The PMA encompasses the rover's "head" and "neck" (see Figure 4). The mast itself is hollow; the Mini-TES instrument, contained within the Warm Electronics Box, uses it as a periscope, with an actuated scanning or "pointing" mirror at the top of the mast that enables Mini-TES to acquire spectra from elevations 30° above the nominal horizon to 50° below it [*Squyres et al.* 2003]. The Navcam and Pancam cameras are mounted on a movable bar above the mast, actuated to enable approximately zenith to nadir (+90 to -97°) elevation coverage by these instruments [*Squyres et al.* 2003]. An azimuth actuator at the base of the mast can rotate the PMA through 370° of azimuth to provide full coverage with slight overlap [*Squyres et al.* 2003].

---

[2] Because the rover is in the southern hemisphere, positions with north-facing normals maximize the solar radiation incident upon the solar arrays. At this time, the team was purposefully planning drives that would land the rover on such a slope at the end of the drive.

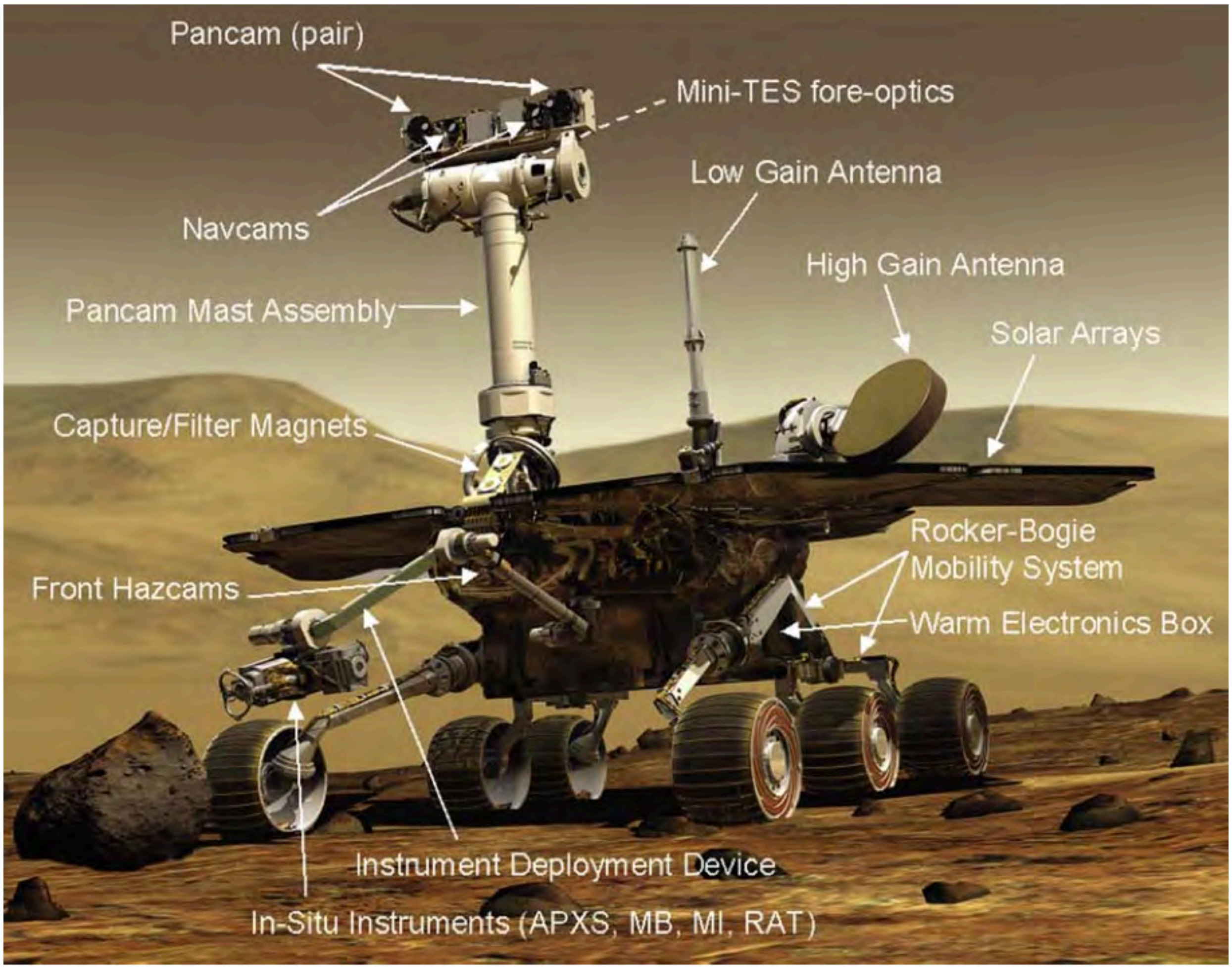

Figure 4. The Mars Exploration Rover, rendered by Maas Digital LLC. Figure 7 from *Crisp et al.* [2003].

2.1.5 Instrument Deployment Device (IDD)

The IDD has roughly the size of a human arm. Shoulder, elbow and wrist joints enable five degrees of freedom: azimuth and elevation at the shoulder, elevation at the elbow, and pitch and rotation at the wrist [*Squyres et al.* 2003]. The in-situ payload elements (MB, MI, APXS, RAT) are mounted on a turret at the end of the wrist (see Figure 4).

2.1.6 Warm Electronics Box (WEB)

Diurnal temperatures on the martian surface vary through nearly 100°C. Electronics respond poorly to such thermal conditions. A Warm Electronics Box, mounted underneath the rover deck, protects the rover's temperature-sensitive components, including the Mini-TES instrument and rechargeable batteries, in an environment in which temperatures range from +50°C to -40°C [*Crisp et al.* 2003, *Christensen et al.* 2003]. This is accomplished through a combination of insulation, waste heat from the electronics, radioisotope heater units, and auxiliary survival heaters [*Crisp et al.* 2003].

2.2 The Athena Science Payload

The instrument suite comprising the Athena Science Payload is designed to enable MER researchers to analyze the geology, mineralogy, and geochemistry of the rover's immediate environment. Additional instruments (Navcam, Hazcam) were included on the rovers for engineering purposes, but in practice are widely used for scientific purposes as well, and so are included here. Rock textures and morphology, as observed at outcrop, hand sample, and microscopic scales, can constrain the depositional environment of the now-lithified material. Different minerals form under different conditions (*e.g.*, redox state, pH, element/component availability, water activity); by analyzing a mineral assemblage, one can constrain environmental conditions. By combining textural, mineralogical, and geochemical data across a region, such as Husband Hill, we can reconstruct the geologic, and therefore environmental, history of that area.

To this end, the rover is instrumented with cameras for morphology at outcrop and hand sample (Navcam, Pancam, Hazcam) and microscopic (Microscopic Imager) scales; spectrometers for mineralogical (Pancam, Mini-Thermal Emission Spectrometer, Mössbauer Spectrometer) and geochemical (Alpha Particle X-ray Spectrometer, Mössbauer Spectrometer) analyses, and a device (Rock Abrasion Tool) to provide clean and/or fresh surfaces for analysis. I describe each payload element below. Due to the engineering and physics underlying these instruments' operations, they do not necessarily sample the same target: their spatial resolution and penetration depths do not always coincide (see Table 2). The instruments are either mounted on the Pancam Mast Assembly (PMA) for remote sensing of distant targets, or on the Instrument Deployment Device (IDD) for *in situ* measurements on targets up to a few cm from the instrument's detector.

2.2.1 Panoramic Cameras (Pancam)

Information in this section is from *Bell et al.* [2003] unless otherwise indicated.

Pancam, the rover's main scientific camera, is both an imaging spectrometer and a stereo camera. The work described in this thesis makes extensive use of stereogrammetry, quantitative measurements of spatial relations derived from co-registered pixels, in Pancam stereo image pairs. Mineralogical information derived from Pancam multispectral data is used to a lesser extent.

2.2.1.1 Camera System and Optics

The Pancam instrument consists of a pair of 1024 x 2048 pixel CCD cameras, each with a 16° x 16° field of view, separated by a distance of 30 cm with a 1° toe-in for stereo parallax with 100% overlap of the right and images for targets at 10m distance (see Figure 5). Half of the CCD array (1024 x 1024 pixels) is the active imaging area; the other half is a masked storage/readout area. The system is fixed focus, with an effective focal length of 43 mm and a focal ratio of *f*/20, resulting in a resolution of 0.27mrad/pixel, equivalent to the human eye's 20/20 vision, with best focus at distances from 3 m from the rover to infinity, and good focus at 1.5 m. The camera lens is a Cooke triplet with essentially no measurable distortion. The lenses and filter wheels are protected from dust and stray and scattered light by a sapphire window with an antireflection coating; a sunshade above the camera and black internal baffles provide extra protection against stray and scattered light.

Table 2. Summary of Mars Exploration Rover payload elements. Data are from *Bell et al.* [2003] (Pancam), *Maki et al.* [2003] (Navcam and Hazcam), *Christensen et al.* [2003] (Mini-TES), *Herkenhoff et al.* [2003] (MI), *Rieder et al.* [2003] (APXS), *Klingelhoefer et al.* [2003] (MB), and *Gorevan et al.* [2003] (RAT). Estimated Pancam penetration depth is from *Elachi* [1987].

Payload element	In situ or remote sensing	Scientific Purpose	Field of View	Sampling Depth	Spatial Resolution	Spectral Resolution
Pancam	Remote sensing	Reconnaissance, outcrop-scale, and hand-sample-scale color imaging; VNIR spectroscopy	16° x 16°	~30 µm	0.27 mrad/pixel	~30-70 nm
Navcam	Remote sensing	Reconnaissance and auto-navigation imaging	45° x 45°	–	0.82 mrad/pixel	–
Hazcam	Remote sensing	Hazard avoidance and near-field imaging	124° x 124°	–	2.1 mrad/pixel	–
Mini-TES	Remote sensing	Mineralogy and thermophysical properties	20mrad; 8mrad with field stop	~40-50 µm of weathering rind/ dust; 1st mineral scattering surface	Single pixel	9.99 cm^{-1}
MI	In situ	Fine-scale imaging	31 x 31 mm		31 µm/pixel	–
APXS	In situ	Elemental chemistry	38 mm circle	~3-100 µm (varies by element)	Single "pixel"	160 eV
MB	In situ	Iron mineralogy	14 mm circle	Solid basaltic rock: ~50-200µm Dust: ~500-2000 µm	Single "pixel"	1.0-1.5keV at room temperature (improves with lower temperatures)
MAGNETS	–	Enable analysis of magnetic fines by payload instruments	–	–	–	–
RAT	In situ	Cleaning targets of dust; producing fresh rock surfaces	45 mm	Up to several mm, depending on rock hardness	–	–

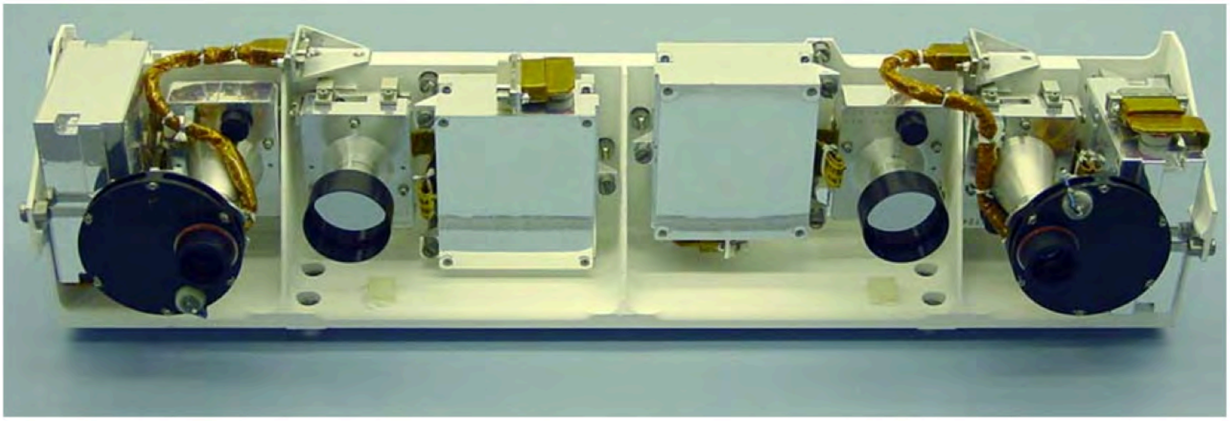

Figure 5. The Pancam and Navcam cameras on the Pancam Mast Assembly (PMA) camera bar. The stereo Pancam and Navcam cameras are separated by 30 cm and 20 cm, respectively. Figure 6 from *Maki et al.* [2003].

After image acquisition, charge is transferred from the imaging area of the CCD to the storage/readout area; this transfer takes 5.1 ms. Pixels are then read out row by row, at a rate of 5.1 ms per row, from the storage area into a serial register. The register includes an additional 16 pixels at each end that are read out along with the image pixels, which can be saved to provide data about the bias level of the image. The 5.1 ms per row readout rate limits the image acquisition rate to ~5 seconds per image. This lag can noticeably affect the position of dust devils when multiple filters are used to produce color images.

2.2.1.2 Stereogrammetry

This thesis makes extensive use of stereogrammetry, a technique that extracts quantitative 3-D information from the parallax observed in stereo image pairs. This is distinct from photoclinometry, which uses variations in scene radiance and a photometric model to estimate variations in slope across a (non-stereo) scene.

The Multimission Image Processing Laboratory (MIPL) at the Jet Propulsion Laboratory (JPL) processes MER image data. This includes producing “disparity maps” from stereo image pairs (see Table 3). An automated correlator compares left- and right-“eye” images, pixel by pixel, in search of objects that can be identified in both images. The correlator then records the location of the corresponding right-eye (by convention) pixels in a disparity map image file [*Maki et al.* 2003]. The disparity map data can be combined with geometric models of the MER cameras to produce “XYZ” images, which record the location of each correlated pixel in 3D space; the XYZ image can be used to produce a “range map” showing the distance between the rover and the location represented by each pixel [*Maki et al.* 2003]. The study described in Chapter 5 makes extensive use of XYZ image files. Range maps and range error maps, which represent the uncertainty in the ranging for each pixel, were used as quality control to ensure measured layer traces represented the actual curve of an observed plane, rather than being dominated by uncertainty in the positions of the pixels composing the trace.

The geometric models of the MER cameras can also be used to produce “linearized” images (see Table 3), in which pixels are reprojected to remove nonlinear spatial distortions and to align stereo images such that correlated pixels within a row in the left-eye image will be constrained to a single row in the right-eye image (epipolar alignment) [*Maki et al.* 2003]. This reduces the time required by the stereo correlation process, but can introduce errors that reduce accuracy of fine-scale correlations such as those used in Chapter 5 [*Hallie Gengl,* personal communication]. I do not use linearized images in the study described in Chapter 5.

Table 3. Types of Reduced Data Records (RDR) images produced by the MER Ground Data System (GDS). Adapted from Table 10 of *Maki et al.* [2003].

Name	Description
Linearized image	Reprojected image, geometric lens distortion removed and stereo pairs epipolarly aligned
Stereo disparity images	Images that contain the row/column pixel values describing the relationship between the location of an object in the right image and its corresponding location in the left image of a stereo pair, stored as two arrays of floating point numbers. These images, along with the corresponding camera model, are used to triangulate the 3-dimensional position of a pixel in Cartesian space.
XYZ image	Image that contains the triangulated 3-dimensional location of an image pixel in Cartesian space, stored as a 3-banded floating point image array
Range map	Image that contains the camera-to-object distance of a pixel in an image, stored as a floating point number

Table 4. Pancam Filter Characteristics. Table 4 from *Bell et al.* (2003).

Name	λ_{eff}, nm	Band Pass, nm	Comment
		Left Camera	
L1	739	338	empty slot, no filter
L2	753	20	red stereo L
L3	673	16	geology
L4	601	17	geology
L5	535	20	geology
L6	482	30	geology
L7	432	32	blue stereo L
L8	440	20	solar ND5
		Right Camera	
R1	436	37	blue stereo R
R2	754	20	red stereo R
R3	803	20	geology
R4	864	17	geology
R5	904	26	geology
R6	934	25	geology
R7	1009	38	geology
R8	880	20	solar ND5

2.2.1.3 Visible and Near-Infrared (VNIR) reflectance spectroscopy

In addition to being a color stereo camera, Pancam is a multispectral Visible and Near-Infrared (VNIR) imaging spectrometer. It is sensitive to the wavelength range ~430 – 1000 nm (see Figure 6 and Table 4), which corresponds to energies of ~1.25 – 3 eV; this is the range that

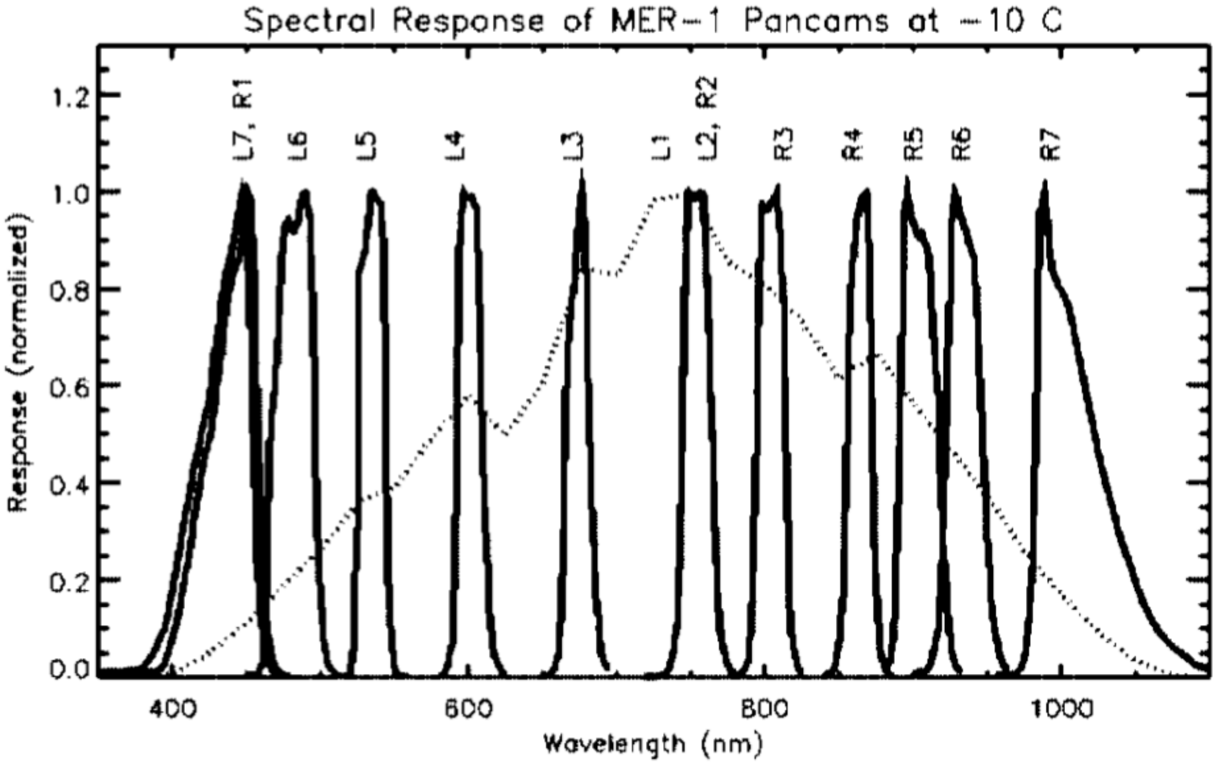

Figure 6. Normalized transmission profiles of the Pancam geology filters. Adapted from Figure 6 of *Bell et al.* [2003].

Table 5. Reasoning behind Pancam geology filter selection. Information is from *Bell et al.* [2003].

Spectral feature	*Geologic significance*
Near-UV to visible ferric absorption edge from ~440 nm to 750 nm	Slope is an indicator of ferric mineral crystallinity
Crystaline ferric oxide absorption features centered near ~650 nm and 860 to 900 nm	Band centers are diagnostic of oxide versus oxyhydroxide compositions
Short wavelength wing of "1 μm" absorption band in ferrous silicates (*e.g.* pyroxene)	Band shape and position are diagnostic of the specific pyroxene (Ca, Fe, Mg) chemistry

separates the electronic energy levels in incompletely filled *d* and *f* orbitals of transition metal cations [*Burns* 1993]. Iron, either as Fe^{2+} or Fe^{3+}, is the most common transition metal in geological material. Pancam multispectral data, therefore, can be interpreted in terms of iron minerals including olivine, pyroxenes, oxides, and oxyhydroxides (see Table 5) [*Bell et al.* 2003].

A rotatable filter wheel is positioned in front of each camera, enabling the acquisition of images at specified wavelengths, stereo imagery with blue or red filters, solar observations, and multispectral VNIR imaging spectroscopy. The 13 geological filters, spread across the two cameras (see Table 4), were selected to enable the detection and quantification of the abundances of ferrous and ferric phases (see Table 5); the two cameras have overlapping red and blue filters (L2/R2 and L7/R1, respectively) for stereo imagery.

2.2.1.4 Calibration and data processing

The Pancam calibration target is located on the rover's rear solar panel (see Figure 8). It includes silicone-based color chips containing hematite (red), chromium oxide (green), goethite (yellow), and cobalt aluminate (blue) pigments; silicone-based gray level annuli with 20%, 40%, and 60% reflectivity; and a vertical post whose shadowed region enables the quantification of direct versus diffuse radiance, and also functions as a sundial. Polished aluminum partial annuli reflect the color of the sky. Reflectivity of the calibration target was characterized with respect to both wavelength and temperature before launch.

Pre-flight camera calibration included imaging of the flight calibration target by all four flight Pancam cameras, through the filters, during thermal vacuum tests. Reflectances of each reference area (four color chips and three grey level annuli) of the calibration target were characterized with a hyperspectral laboratory spectrometer. Incidence angle effects on radiance

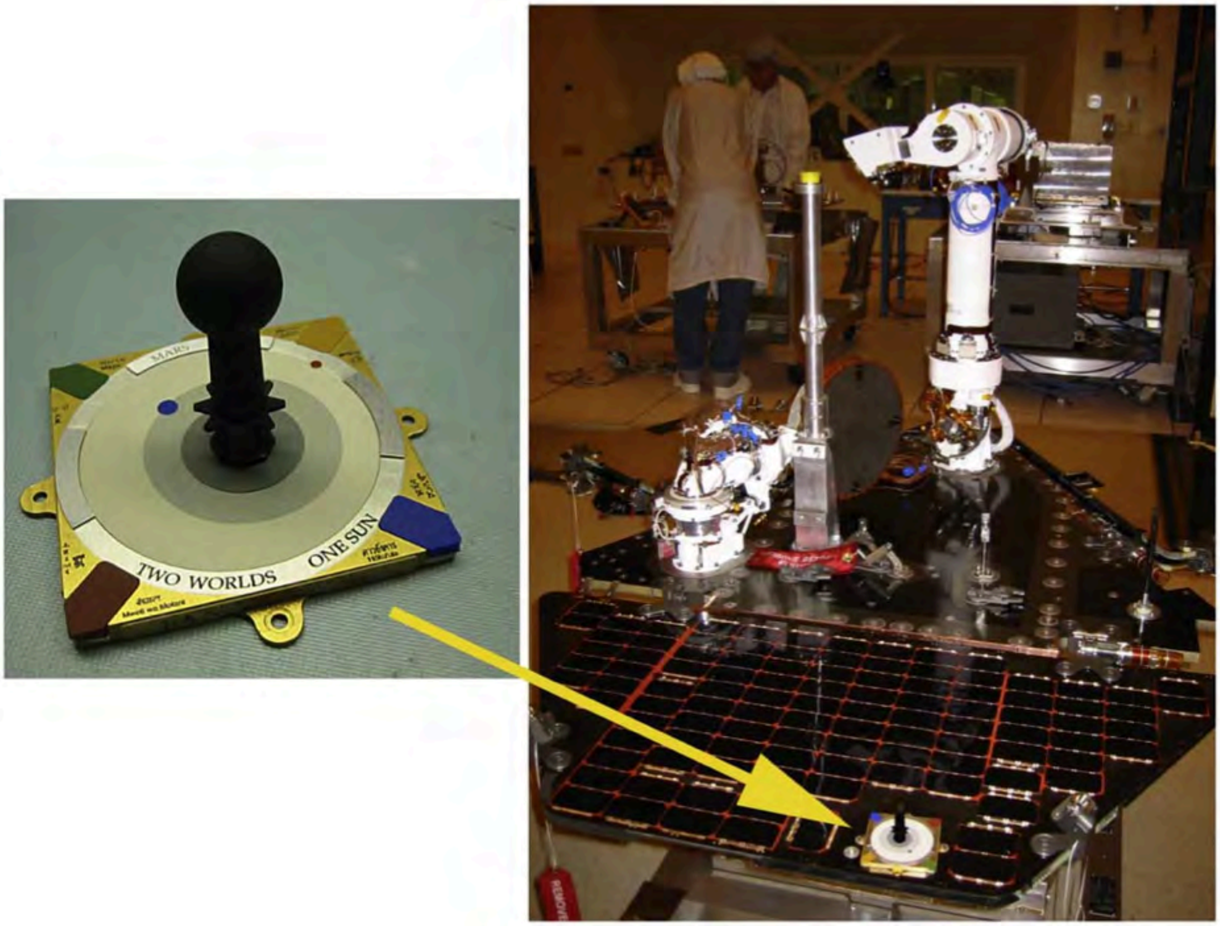

Figure 8. The Pancam Calibration Target. The base is 8 x 8 cm, and the shadow post, which also acts as a sundial, is 6cm high. The blue and red dots on the gray level annuli represent Earth and Mars. Figure 7 from *Bell et al.* [2003].

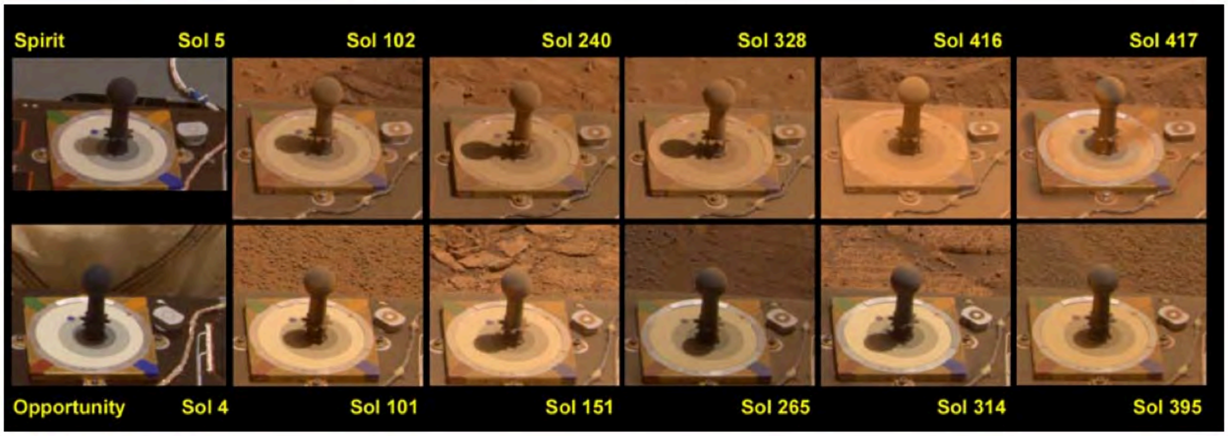

Figure 7. Approximate true color images of Spirit's (top) and Opportunity's (bottom) calibration targets throughout the first ~400 sols of the mission. Opportunity experienced frequent, small gusts of wind at Meridiani, which kept the rover relatively clean. The Gusev environment is dustier, and Spirit experienced occasional, strong wind events; the first occurred between the images above taken on Sols 416 and 417. Figure 19 from *Bell et al.* [2006].

were modeled based on laboratory measurements including 169 incident-azimuth-elevation orientations, with emission fixed at a 53.5° angle representing the Pancam viewing angle of the calibration target on the rover. Geologic standards and prepared rock targets, including a variety of geologic materials that could be encountered on Mars, were imaged during thermal vacuum testing. These targets were characterized with standard laboratory techniques, and many were also imaged by Navcam, Hazcam, and MI cameras and analyzed by the Mini-TES, APXS, and Mössbauer spectrometers.

Each CCD has a temperature sensor, as does the left Pancam electronics box. The camera's detector head and electronics box are thermally isolated from each other, enabling heating of the electronics without warming the CCD, which could induce dark current [*Maki et al.* 2003]. The filter wheels and electronics are capable of operating within the temperature range -60°C – +45°C and -60°C – +55°C, respectively; the CCDs are calibrated for the temperature range -55°C – +5°C. Each electronics box and filter wheel is instrumented with a heater, but the CCDs are not, and their temperatures vary with the local environment, necessitating a temperature reading for the CCDs and electronics for proper image calibration.

Onboard flight software calibration and data processing capabilities include corrections for bad pixels (those always saturated with dark current), hot pixels (those that acquire charge far faster than the majority) in the imaging and storage regions of the CCD, detector bias signal, dark current in the imaging and frame transfer regions of the CCD, flatfield (pixel-to-pixel responsivity), and frame transfer smear; image downsampling (*e.g.*, for 64 x 64 pixel "thumbnail" images); image subframing; pixel summing; 12 to 8 bit re-encoding via lookup tables; and multiple forms of image compression [*Bell et al.* 2006]. Images are compressed using ICER, a progressive wavelet-transform compressor that can be lossy or lossless depending on user inputs, or with the faster "LOCO" compression, which is lossless [*Maki et al.* 2003].

Pancam data are radiometrically calibrated for use in VNIR spectroscopy, and for generating approximate true-color images. The automated Pancam calibration pipeline generates "RAD" images, in which the data have been converted to scene radiance in units of $W/m^2/nm/sr$. Pancam image acquisition sequences are typically accompanied by images of the calibration target taken with each filter used in the image sequence, under similar lighting conditions. Human "calibration analysts" examine RAD images of the target, selecting regions of interest from each of the color and gray level regions, and calibrate the images based on the pre-flight characterization and the known angle of the Sun during image acquisition [*Bell et al.* 2006]. A Hapke scattering model is used to correct for dust deposition upon the calibration target (see Figure 7) [*Bell et al.* 2006]. RAD (radiance products) have an estimated accuracy of ~10%; the accuracies of IOF (reflectance products) are estimated to be ~10% or less for spectral shape, 1-5% filter-to-filter, and <1% pixel-to-pixel [*Bell et al.* 2006].

2.2.1.5 Image products

Pancam routinely acquires sub-frame and full-frame images, often acquires multi-frame mosaics, and occasionally acquires 360° panoramas. Due to data volume – each rover's memory is the equivalent of a 256MB USB stick – and downlink data volume constraints, 13-filter (13F) imaging is restricted to carefully selected targets. Images may be acquired with filters selected for approximate true color, false color, and/or stereo. Typical Pancam products include images acquired with individual filters; stereo anaglyphs; digital terrain models; approximately true color images produced with the L27 filters; and false-color images that enhance subtle color variations, produced with the L257 filters. Radiometrically calibrated images are archived as "RAD" files, and calibrated reflectance images are archived as "IOF" files. A "tau", or image of the Sun using the solar filters, is acquired nearly every sol; this atmospheric observation is used to estimate the atmospheric opacity, which varies with the amount of dust in the martian atmosphere.

Stereo image data can be processed into anaglyphs and digital terrain models for use in stereogrammatic analyses such as that in Chapter 5. In addition to the "standard" false color images, multispectral image data can be used to display spectral parameters including band depth, band ratios, spectral slopes, Principle Components Analysis (PCA) results, etc. [*c.f.,* Farrand et al. 2006, 2008].

Pancam data products are archived as raw Experiment Data Records (EDRs) and calibrated Reduced Data Records (RDRs) on the Planetary Data System (PDS) at http://pds-geosciences.wustl.edu/missions/mer/geo_mer_datasets.htm. The latter are the standard Pancam data products, and are calibrated to radiance. Headers in all EDR and RDR files include a large amount of mission, instrument, telemetry, and data product metadata. The appendices of *Bell et al.* [2006] provides a glossary of terms used in Pancam PDS headers and MER file-naming conventions.

Approximate true color and false color JPEG images are generated automatically and uploaded to a public website (http://marswatch.astro.cornell.edu/pancam_instrument/images.html) upon downlink. Mosaics and panoramas, in approximate true color and/or false color and/or anaglyph format, are uploaded to the site when they are produced.

2.2.2 Miniature Thermal Emission Spectrometer (Mini-TES)

Information in this section is from *Christensen et al.* [2003] unless otherwise indicated.

Mini-TES is a hyperspectral thermal infrared (TIR) spectrometer. It is the rover's primary remote sensing mineralogy instrument, and can be used to survey rocks within ~10 m of the rover; those with new compositions may be selected for in-depth examination with the IDD instruments. While rock classes are defined by APXS elemental abundances, they can be identified from afar by Mini-TES. In addition, the instrument can make thermophysical measurements such as surface temperature and thermal inertia, which often correlates with particle size; and atmospheric measurements such as temperature profile, water vapor abundance, and dust and water-ice opacity.

2.2.2.1 Thermal Infrared (TIR) emission spectroscopy

Unlike VNIR reflectance spectra, which are primarily influenced by electron energy level transitions in incompletely filled *d* and *f* orbitals of transition metal cations (see Section 2.2.1.3), TIR spectra, also known as emission spectra and mid-infrared spectra, are the result of vibrational energy level transitions within crystal lattices, which depend on both the structure and the composition of the crystal lattice. Lattice vibrations are typically caused by the stretching or bending of bonds between atoms. Tighter bonds require more energy to bend, and therefore correspond to absorptions at shorter wavelengths. Factors affecting bond strength include polymerization and tetrahedral arrangement (*e.g.*, sheet, chain, or framework silicate structure), coordination number, and anion group composition [*Christensen et al.* 1992]: silicates, carbonates, phosphates, sulfates, oxides, and hydroxides each have diagnostic vibrational spectral bands in the TIR region, with specific signatures corresponding to specific compositions (*e.g.*, Mg-rich vs. Fe-rich olivine) within these mineral groups (see Figure 9). The Mini-TES instrument was required to be capable of determining mineral abundances in mixtures to within 5% absolute abundance.

2.2.2.2 Quantitative modeling of mineralogy

Because mineral absorption coefficients are quite strong for wavelengths in the TIR region, TIR photons do not tend to penetrate mineral grains as VNIR photons do [*Ramsey and Christensen* 1998]. VNIR spectra of geologic targets are dominated by volume scattering: photons may interact with several grains and interfaces before reaching the detector, allowing minerals with low abundances but relatively high absorption coefficients to have a significant impact on the

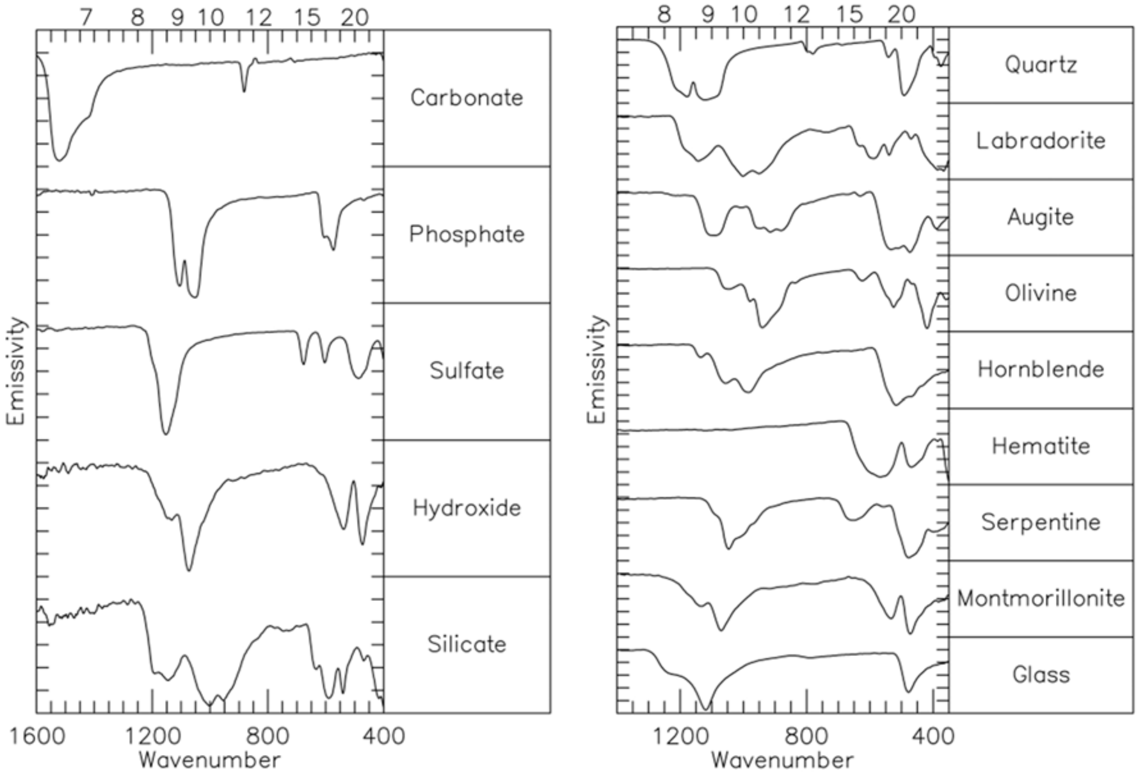

Figure 9. Thermal emission spectra of mineral groups (left) and individual minerals (right). Figures 3 and 4 from *Christensen et al.* [2003].

measured spectrum. TIR spectra of geologic targets, on the other hand, are dominated by surface scattering: incident photons tend to experience only a single interaction with a geologic target before either being emitted from the target and potentially reaching the detector, or being absorbed by a mineral grain [*Ramsey and Christensen* 1998]. A TIR spectrum is therefore a linear combination of the spectra of the target's components, with the amplitude of each component's spectrum corresponding to the areal percentage of that component in the detector's field of view.

A spectral deconvolution method has been established to quantitatively model mineral abundances of terrestrial and martian rock targets [*Christensen et al.* 2004, *Feely and Christensen* 1999, *Glotch and Banfield* 2006, *Glotch et al.* 2006, *Hamilton et al.* 1997, *Hamilton and Christensen* 2000, *Ramsey and Christensen* 1998, *Ruff et al.* 2006, *Ruff et al.* manuscript in preparation]. A set of "endmember" spectra is input into the linear deconvolution algorithm, along with the target spectra to be deconvolved. The endmember spectra are typically laboratory measurements of individual minerals, but can also include more complex spectra, such as martian dust [*Ruff et al.* 2006] or rock targets [*Ruff et al.*, manuscript in preparation]. The algorithm deconvolves the target spectra using a least squares fitting procedure, and outputs the modeled percentage of each spectrum in its final fit, and a root-mean-square (RMS) estimate of the error of the fit. A caveat of this method is that the RMS value is a mathematical calculation, and does not necessarily correspond to the *accuracy* of the modeled set of components for the geologic target. The analyst must use his or her judgment as to whether or not the modeled components are reasonable, and may implement constraints within the deconvolution, such as expanding or constraining the input spectral end members. In MER Mini-TES analyses, elemental abundances derived from APXS measurements can provide constraints.

2.2.2.3 Atmospheric observations and thermophysical measurements

Atmospheric observations included "elevation scans", in which spectra were acquired at multiple elevations, and "stares", which acquired data at one elevation for an extended period of time [*Smith et al.* 2006]. The elevation scans enabled the analysis of different air masses, while stares examined temporal variations on scales from two seconds through ~1 hr. Atmospheric observations result in temperature profile measurements of the lower ~2 km of the planetary boundary layer, including diurnal variations in atmospheric and effective surface temperatures; seasonal trends in atmospheric temperatures, dust opacity, and water vapor abundance; and atmospheric temperature profile variations on 15-60 second scales, associated with turbulence and convection [*Smith et al.* 2006].

Thermophysical measurements are acquired at multiple times of day in order to model thermal inertia. Surface temperatures are modeled from spectra by fitting a Planck function to the calibrated radiance at each wavelength, and assigning the warmest brightness temperature as the target temperature [*Fergason et al.* 2006]. Thermal inertia of bedform, soil and rock targets, provide data on soil and bedform particle sizes and rock porosity [*Fergason et al.* 2006].

2.2.2.4 The Mini-TES Instrument

Mini-TES is a miniaturized version of the Thermal Emission Spectrometer (TES) instrument [*Christensen et al.* 1992] that flew on the Mars Observer (MO, launched in 1992) and Mars Global Surveyor (MGS, launched in 1996) missions. Mars Observer did not achieve orbit, but MGS conducted a highly successful mission from September 1997 through November 2006.

The majority of the Mini-TES instrument is located with the rover's Warm Electronics Box, and the instrument uses the PMA as a periscope. Infrared radiation enters the Mini-TES through an aperture just below the PMA's camera bar (see Figure 4). The optical path begins with an actuated pointing mirror, located behind the aperture, and a fixed fold mirror. It continues down the PMA, which is instrumented with a 6.35 cm diameter primary mirror and a 1.12 cm diameter secondary mirror, and thus functions as a Cassegrain telescope, and into the Michelson interferometer. Schematics of the optical system are shown in Figure 10. The pointing mirror enables observations with elevations from 50° below the nominal horizon, corresponding to terrain ~2 m from the rover, to 30° above the nominal horizon, for atmospheric measurements. PMA rotation enables observations at any azimuth.

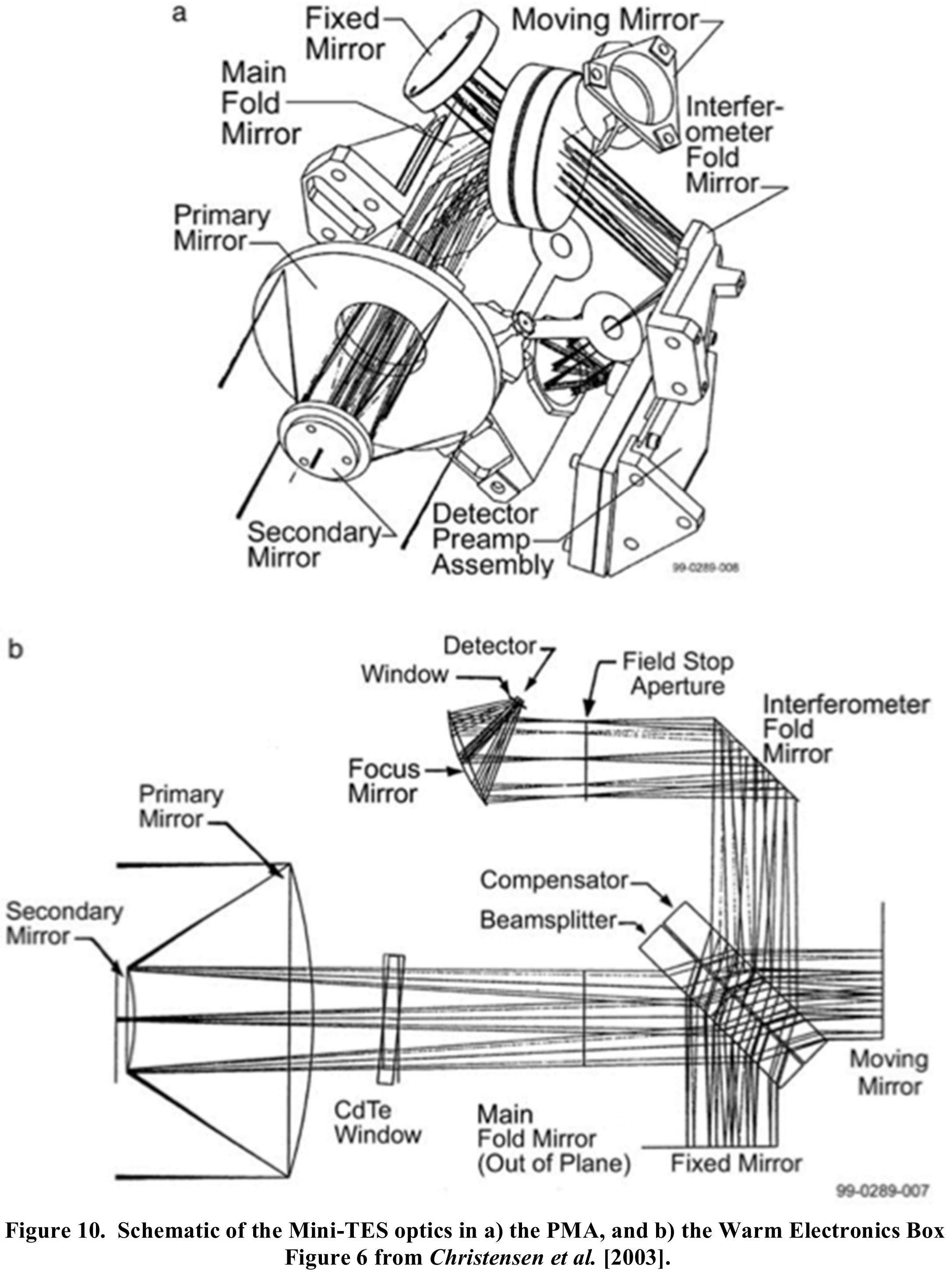

Figure 10. Schematic of the Mini-TES optics in a) the PMA, and b) the Warm Electronics Box. Figure 6 from *Christensen et al.* [2003].

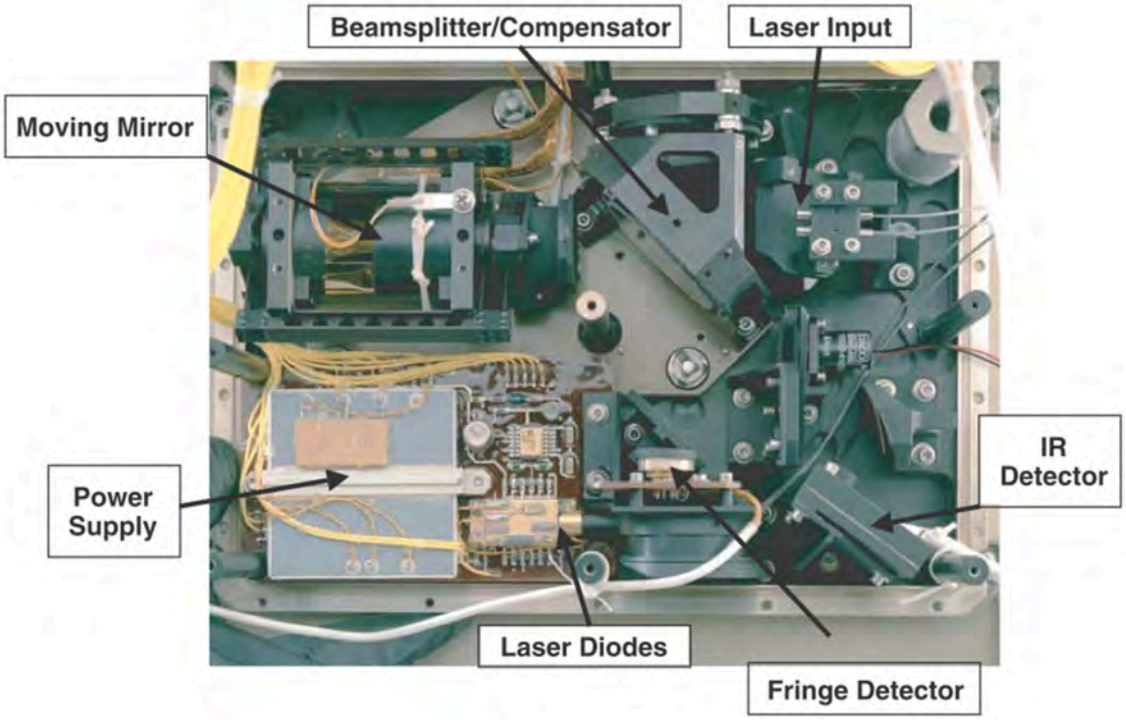

Figure 11. The Mini-TES components in the Warm Electronics Box. Figure 8 from *Christensen et al.* [2003].

Mini-TES covers a spectral range of 5-29.5 μm (1997.06 - 339.50 cm^{-1}) with a spectral sampling of 9.99 cm^{-1}. The nominal Mini-TES field-of-view is 20 mrad; an actuated field stop can reduce this to 8 mrad. The instrument's Michelson interferometer simultaneously records radiance across the full spectral range as an interferogram, which is processed into spectra by the rover flight software. The mirror at the end of one arm of the interferometer is fixed, and the other moves ±0.25 mm at a constant velocity (see Figure 11). The beamsplitter that directs radiation into the two arms is installed in a radial 3-point mount that maintains alignment over a -50°C to +50°C temperature range. Mini-TES design and performance parameters are shown in Table 6. The rover's flight software processes the interferogram into spectra using a Fast Fourier Transform (FFT) algorithm.

Table 6. Mini-TES design and performance parameters. Table 2 from *Christensen et al.* [2006].

Parameter	Description
Spectral Range	339.50 to 1997.06 cm^{-1} (5.01-29.45) μm)
Spectral Sampling Interval	9.99 cm^{-1}
Field of View	8 and 20 mrad
Telescope Aperture	6.35-cm-diameter Cassegrain
Detectors	Uncooled Alanine doped Deuterated Triglycine Sulphate (ADTGS) Pyroelectric detector
Michelson Mirror Travel	-0.25 to 0.25 mm
Mirror Velocity (physical travel)	0.0325 cm/sec
Laser Fringe Reference Wavelength	978 ± 2 nanometers
Interferometer Sample Rate	645 samples/sec
Cycle Time per Measurement	2 seconds (1.8 seconds Michelson mirror forward scan; 0.2 second retrace)
Number of Scans to Achieve 400 SNR at 1000 cm^{-1}; 270 K Scene Temp; 0°C Instrument temp	2 (20 mrad); 80 (8 mrad)
Number Samples per Interferogram	1024
Number Bits per Sample - Interferogram	16
Number Samples per Spectrum	167
Number Bits per Sample - Spectrum	12
Dimensions	23.5 x 16.3 x 15.5 cm
Mass	2.40 kg
Power	5.6 W (operating), 0.3 W (daily average)
Operational Temperature Range (Instrument Temperature)	Survival and Operability -45, +50°C; Performance within Spec -10, +30°C

Typical observations of geological targets consist of 200 spectral scans (interferograms) acquired at the same pointing, which, along with observations of the internal calibration target (see Section 2.2.2.5). The data are sent to the rover's computer at a rate of one interferogram every two seconds. The individual spectral scans can later be summed to increase signal to noise.

2.2.2.5 Calibration

The Mini-TES spectrometer was calibrated pre-flight both with and without the PMA. The spectrometer itself was tested and calibrated in vacuum at instrument temperatures of -30°C, -10°C, +10°C, and +30°C. Two precision calibration reference blackbody standards were in the field of view, set independently at several temperatures ranging from 223K to 283K and 145K to 345K, respectively. The Mini-TES/PMA assembly was radiometrically calibrated at instrument temperatures of -30°C, 0°C, and +30°C in 6mbar of nitrogen, with calibration blackbody temperatures ranging from 145K to 325K; the radiometric precision was determined to be ±1.8 x 10^{-8} W cm^{-2} sr^{-1}/cm^{-1} in the wavenumber range 450-1500 cm^{-1} at normal operating instrument and target temperatures, assuming two spectra per observation. The absolute error under these conditions was determined to be ~1 x 10^{-8} W cm^{-2} sr^{-1}/cm^{-1}, for a worst case absolute temperature error of ~0.4K and ~1.5K for target surfaces at 270K and 180K, respectively. This corresponds to a smoothly varying offset in the emissivity spectrum that does not impact the modeled composition of the target. The temperature-dependent instrument response function was derived from measurements of one hot and one cold calibration blackbody during thermal vacuum testing.

Each rover is instrumented with two Mini-TES calibration targets: one on the rover deck, and the other mounted inside the PMA. The targets are machined from aluminum alloy, with parallel grooves 1.73 mm deep and spaced 1.2 mm apart, machined with 15° inclined surfaces. The surface is painted with a ~6 mil thickness of Aeroglaze Z302 black paint. The calibration targets' emissivities were measured during thermal vacuum testing, and the external targets' emissivities were additionally measured at the ASU Thermal Spectroscopy Lab. Two thermistors are bonded to the bottom of each calibration target to measure its temperature. The manufacturer measured the absolute accuracy of the thermistors to be better than 0.1°C for the temperature range -130°C to +110°C. During thermal vacuum tests at JPL, the two thermistors on each calibration target were found to agree to <0.5°C over the instrument operating temperatures.

During Spirit's first night on Mars, temperatures reached ~-90°C, causing the thermistors on the external calibration target to fail [*Christensen et al.* 2004]. A calibration scheme was developed that uses the instrument response function measured during pre-flight thermal vacuum testing in conjunction with the internal calibration target and the measured detector temperature of each observation [*Ruff et al.* 2006].

2.2.2.6 Data processing

Information in this section is from *Ruff et al.* [2006] unless otherwise indicated.

The radiance detected by Mini-TES encompasses more than that emitted by a geologic target. In order to extract spectral information for a geologic target, one must remove these additional contributions.

CO_2, the major component of the martian atmosphere, has a strong band centered on 667 cm^{-1} (15μm), which can manifest as an absorption trough or an emission peak depending on whether the target is warmer or cooler than the atmosphere between the target and the detector. Mini-TES analyses typically exclude the range ~560-780 cm^{-1}, as this feature dominates spectra in this region.

Thermal radiation from the sky that illuminates the surface and reflects or scatters into the Mini-TES field of view is known as "downwelling radiance". Its intensity varies with the amount of dust in the atmosphere and the atmospheric temperature. In order to correct for downwelling radiance, Mini-TES atmospheric observations are routinely acquired at an elevation of ~30° above the horizon. The MER "standard downwelling correction" subtracts this atmospheric radiance from that of the target and from the Planck radiance at the maximum brightness temperature of the target, before deriving the target's emissivity. Additional downwelling corrections are discussed in *Ruff et al.* [2006].

2.2.2.7 Mirror-dust correction

On Sols 419-420, aeolian activity, likely linked to the event that removed dust from the solar panels, deposited dust on the Mini-TES pointing mirror. Data acquisition continued, but interpretation was complicated by temperature-dependent emission and absorption spectra of the dust within the optical path. The effect was non-linear, and qualitative analysis focused on the region <~600 cm^{-1} (>~16.7 µm) [*Ruff et al.* 2006], where the dust spectrum is relatively flat [*Christensen et al.* 2004]. A correction, based on radiative transfer, was eventually developed [*Smith et al.* 2006] and incorporated into Mini-TES data analysis [*Ruff et al.* 2011, *Ruff et al.*, manuscript in preparation]. The Mini-TES spectra discussed in Chapter 6 have been corrected for mirror dust [*Ruff et al.*, manuscript in preparation].

2.2.2.8 Spectral libraries

The primary spectral library used to analyze Mini-TES data is the Arizona State University (ASU) Spectral Library [*Christensen et al.* 2000], available online at http://speclib.asu.edu/. The library encompasses laboratory measurements of hundreds of sieved pure mineral samples, rock samples, and martian meteorites. Each spectrum is accompanied by a description that includes compositional and sample quality information. Information about the library can be found at http://tes.asu.edu/spectral/library/index.html.

2.2.2.9 Data products

Mini-TES data products are archived as Radiance and Interferogram Experiment Data Records (EDRs), Radiometrically Calibrated Radiance Reduced Data Records (RDRs), Brightness Temperature Records (BTRs), and Emissivity Records (EMRs), on the Planetary Data System (PDS) at http://pds-geosciences.wustl.edu/missions/mer/geo_mer_datasets.htm. Headers in all files include a large amount of mission, instrument, telemetry, and data product metadata.

2.2.3 Microscopic Imager (MI)

Information in this section is from *Herkenhoff et al.* [2003] unless otherwise indicated.

A field geologist on Earth carries a handlens to examine the microtexture, fabric, and grain size of rocks, soils, and bedforms he or she encounters. The Microscopic Imager, which is mounted on the IDD (see Figure 12a), performs these functions for the MER robotic field geologist. It has a field of view of 31 x 31 mm, with a scale of 31 μm per pixel at best focus, and can resolve objects 100μm in size (corresponding to very fine sand [*Wentworth* 1922]) and larger. The MI is not a microscope, but rather a “macro” lens with a fixed magnification of 0.4.

2.2.3.1 Optics and imaging system

MI uses the same 1024 x 2048 pixel CCD detector and electronics as all of the other MER cameras (see Section 2.2.1.1). The MI CCD and electronics are instrumented with temperature sensors. As for Pancam, one 1024 x 1024 pixel region is used for image acquisition, and the other is a storage area for readout. Images are acquired with integration times of up to ~1.5 seconds [*Herkenhoff et al.* 2006], determined by an auto-exposure algorithm on a case-by-case basis.

The MI optics include a Cooke triplet with a focal ratio of f/15 and an effective depth of field of ±3 mm. A Schott BG-40 (light blue) filter restricts the spectral response to 400-700 nm, similar to the human eye, with an effective wavelength of 570 nm. The MI has neither a filter wheel nor an illumination source; all images are monochrome, and lit by the Sun only. A sapphire window protects the rest of the optics from damage by contact with the surface or windblown particles (see Figure 12b). A motor-operated Kapton polyimide dust cover protects the optics from dust contamination when not in use.

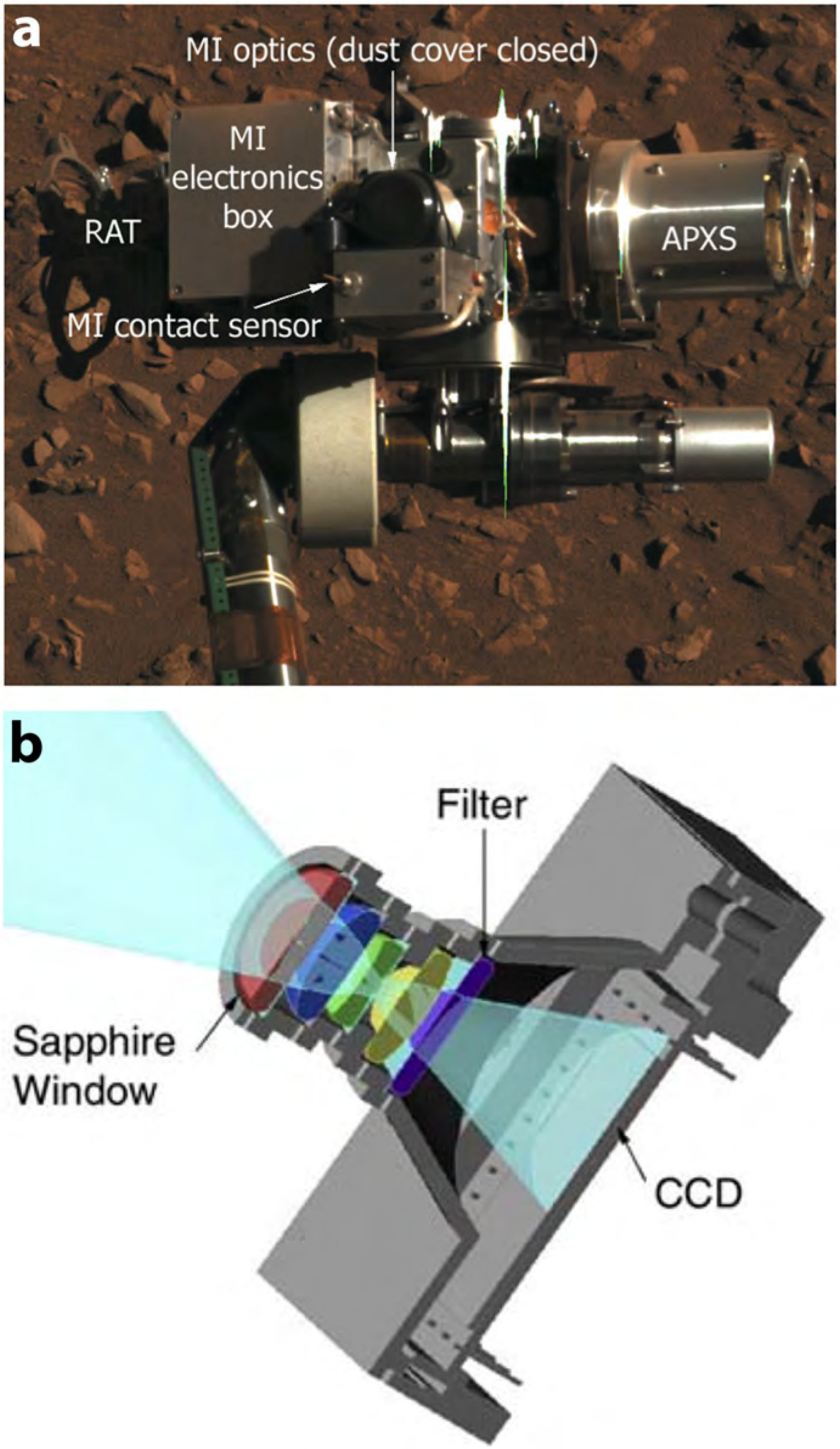

Figure 12. The MER Microscopic Imager. a) Pancam image of Spirit's IDD turret. The turret is ~30 cm across. Sol 287, sequence P2139. Figure 1 from *Herkenhoff et al.* [2006]. b) Schematic of the MI optics. Figure 4 from *Herkenhoff et al.* [2003].

The instrument cannot produce focused images of targets with depth greater than 3 mm. MI images are typically acquired in "stacks" of 3-7 focal section images, in 3 mm intervals perpendicular to the target surface; distance from the target is measured using the Mössbauer or MI contact sensors. An offset image is typically acquired at the height of the middle focal section for stereo coverage. Because many targets' relief exceeds the 3 mm depth of field, each focal section tends to include regions that are in focus and those that are out of focus. The sharpest regions of each image in a stack can be combined into a merged focal image; details of this procedure are described in *Herkenhoff et al.* [2006].

2.2.3.2 Calibration and data processing

Pre-flight thermal vacuum testing of the MI system, without the dust cover, included light transfer, dark current, spectral response, and absolute radiometric calibration. Dark current images were acquired with CCD and electronics temperatures covering the range of expected operational temperatures. These data were used to model multiple sources of dark current generation arising from the camera electronics and CCD temperatures and the exposure time. Dark current images were also acquired during the cruise to Mars with the CCD at -5.4°C and -21.3°C; these were consistent with the model developed during pre-flight calibration [*Herkenhoff et al.* 2006].

Some behavior was tested pre-flight under ambient conditions, including relative ("flat field") radiometric calibration. Blooming behavior was found not to degrade subsequent images. Transfer smear was found to be generated during the CCD flush cycle and image transfer; this effect was modeled to facilitate removing the effect for images that lack the zero-second exposures that are typically used to correct for transfer smear. The resolution and geometric accuracy of the optical system were found to be within design specifications (see Table 7). The

Table 7. MI performance requirements, and measured values for some of these requirements [*Herkenhoff et al.* 2003]. Adapted from Table 1 of *Herkenhoff et al.* [2006].

Parameter	Required value	Measured value
Instantaneous Field of View (IFOV) on-axis	30 ± 1.5 μm/pixel	Spirit: 30.8 μm/pixel Opportunity: 30.7 μm/pixel
Field of View (FOV)	1024 x 1024 square pixels	31.5 mm at the best focus position
Spectral bandpass	400-680 nanometers	
Effective depth of field	≥±3 mm	
Optics MTF over spectral bandpass at best focus	≥0.35 at 30 lp/mm	
Absolute radiometric calibration accuracy	≤20%	
Relative (pixel-to-pixel) radiometric calibration accuracy	≤5%	
Signal to Noise Ratio (SNR) for exposures of ≥20% full well over the spectral bandpass within the calibrated operating temperature range	≥100	
Accuracy of temperature sensor on the CCD package	±2°C	
Working f/#	15 ± 0.75	14.4
Operating temperature range within calibrated specifications	-55 ± 2°C to +5 ± 2°C	

in-flight relative (pixel-to-pixel) radiometric accuracy of well-exposed, calibrated MI data was found to be ±1.5% [*Herkenhoff et al.* 2006].

As with the other cameras, onboard flight software calibration and data processing capabilities include corrections for bad pixels (those always saturated with dark current), hot pixels (those that acquire charge far faster than the majority) in the imaging and storage regions of the CCD, detector bias signal, dark current in the imaging and frame transfer regions of the CCD, flatfield (pixel-to-pixel responsivity), and frame transfer smear; image downsampling (*e.g.*, for 64 x 64 pixel "thumbnail" images); pixel summing; 12 to 8 bit re-encoding via lookup tables; and multiple forms of image compression [*Bell et al.* 2006]. Images are compressed using ICER, a progressive wavelet-transform compressor that can be lossy or lossless depending on user inputs, or with the faster "LOCO" compression, which is lossless [*Maki et al.* 2003].

MI images are corrected for bias, dark current, and flat field sensitivity variations on the ground, and are then radiometrically calibrated to I/F (radiance factor).

2.2.3.3 Image products

MI is capable of acquiring sub-frame images, though that capability is rarely used. Typical MI products include raw and radiometrically calibrated single-frame focal section images, single-frame merged focal images, mosaics, stereo anaglyphs, digital terrain models, and MI/Pancam color merge images. The most common mosaic is two rows by two columns, resulting in a field of view of ~5 cm. Stereo anaglyphs and digital terrain models are produced from stereo pairs resulting from the nominal and offset images acquired at a single distance from the target. MI/Pancam color merges are produced from co-registered MI and Pancam images.

MI data products are archived as Science Image Experiment Data Records (EDRs) and Science Calibrated Image Reduced Data Records (RDRs) on the Planetary Data System (PDS) at http://pds-geosciences.wustl.edu/missions/mer/geo_mer_datasets.htm. The latter are the standard MI data products, and are radiometrically calibrated. Headers in all EDR and RDR files include a large amount of mission, instrument, telemetry, and data product metadata.

Raw MI images, which can be used to measure microscopic features such as particle and grain size, can be found on the Image Gallery page of NASA's Mars Exploration Rovers website: http://mars.jpl.nasa.gov/mer/gallery/all/spirit.html.

MI/Pancam color merges are available on the USGS Astrogeology Science Center Website at http://astrogeology.usgs.gov/maps/mars-mer-mi-merged-products.

2.2.4 Alpha Particle X-ray Spectrometer (APXS)

Information in this section is from *Rieder et al.* [2003] unless otherwise indicated.

The Alpha Particle X-ray Spectrometer is the only instrument on the MER rover capable of detecting the abundance of individual elements. The APXS instrument is mounted on the IDD, and is used to determine the major and minor elemental compositions of geological materials, and to examine variations in atmospheric composition. Rock class definitions are based on APXS-derived elemental abundances.

APXS has nearly 50 years of spacecraft heritage: its first extraterrestrial deployment was on Surveyor V in 1967, and it is the only instrument common to all three generations of Mars rovers to date (Sojourner, the Mars Pathfinder microrover, launched in 1996; Spirit and Opportunity, the Mars Exploration Rovers, launched in 2003; and Curiosity, the Mars Science Laboratory rover, launched in 2011). *Rieder et al.* [1997] provides a history of this instrument from the discovery of Rutherford scattering through its deployment on separate and joint U.S./Soviet spacecraft missions.

2.2.4.1 Alpha Particle X-ray Spectroscopy

The information in this section is from *Rieder et al.* [1997] unless otherwise indicated.

The MER APXS makes use of Rutherford backscattering (RBS), particle-induced X-ray emission (PIXE), and X-ray fluorescence (XRF), though it is optimized for X-ray, rather than alpha, detection. RBE is most sensitive to “light” elements such as C and O, while the X-ray processes are most sensitive to “heavier” elements, the lightest of which is Na. The MER APXS is most sensitive to elements from Na to Br.

The energy of an alpha particle that is scattered off of a target nucleus is a function of the alpha particle's initial energy and scattering angle, and the nuclear mass. For alpha particles emitted with a known energy and backscattered (scattered at an angle of 180°) off of a nucleus, the only unknown is the mass of the target nucleus. In a thick sample, the alphas will lose energy on their paths into and out of the sample, resulting in a range of backscattered energies with a high-energy cutoff equal to the energy of an alpha backscattered off of an isolated target nucleus. The scattering cross-section is a function of the target's nuclear charge and the alpha particle's initial energy and scattering angle. Hence, peak energies in the backscattered alpha spectrum can be used to identify the elements composing a target, and the abundance of each element can be derived from the areas under the peaks.

PIXE is the result of the interaction between an alpha particle and an atom, which can liberate electrons from the K and L shells of the target atom. Electrons from higher-energy shells drop down to fill these vacancies, emitting X-rays with energies characteristic of the element. XRF has the same result, but the K- or L-shell electron is ejected when the atom absorbs an X-ray emitted from the radioactive source. Again the peak energies and subspectral areas can be used to identify elements and quantify their abundances, respectively.

2.2.4.2 The APXS Instrument

The AXPS instrument consists of six ^{244}Cm alpha sources, an X-ray detector, and alpha detectors, encased in a cylindrical enclosure with doors to protect the instrument from dust when not in use. ^{244}Cm decays by alpha particle emission to ^{240}Pu with a half-life of 18.1 years [*Rieder et al.*1997], and thus signal degradation was not expected over the course of the mission. A calibration target, composed of a thin layer of Au over Kapton, is on the interior of the doors. The sources and detectors are arranged coaxially (see Figure 13) on the sensor head, and the electronics are housed in the rover's Warm Electronics Box. The instrument's field of

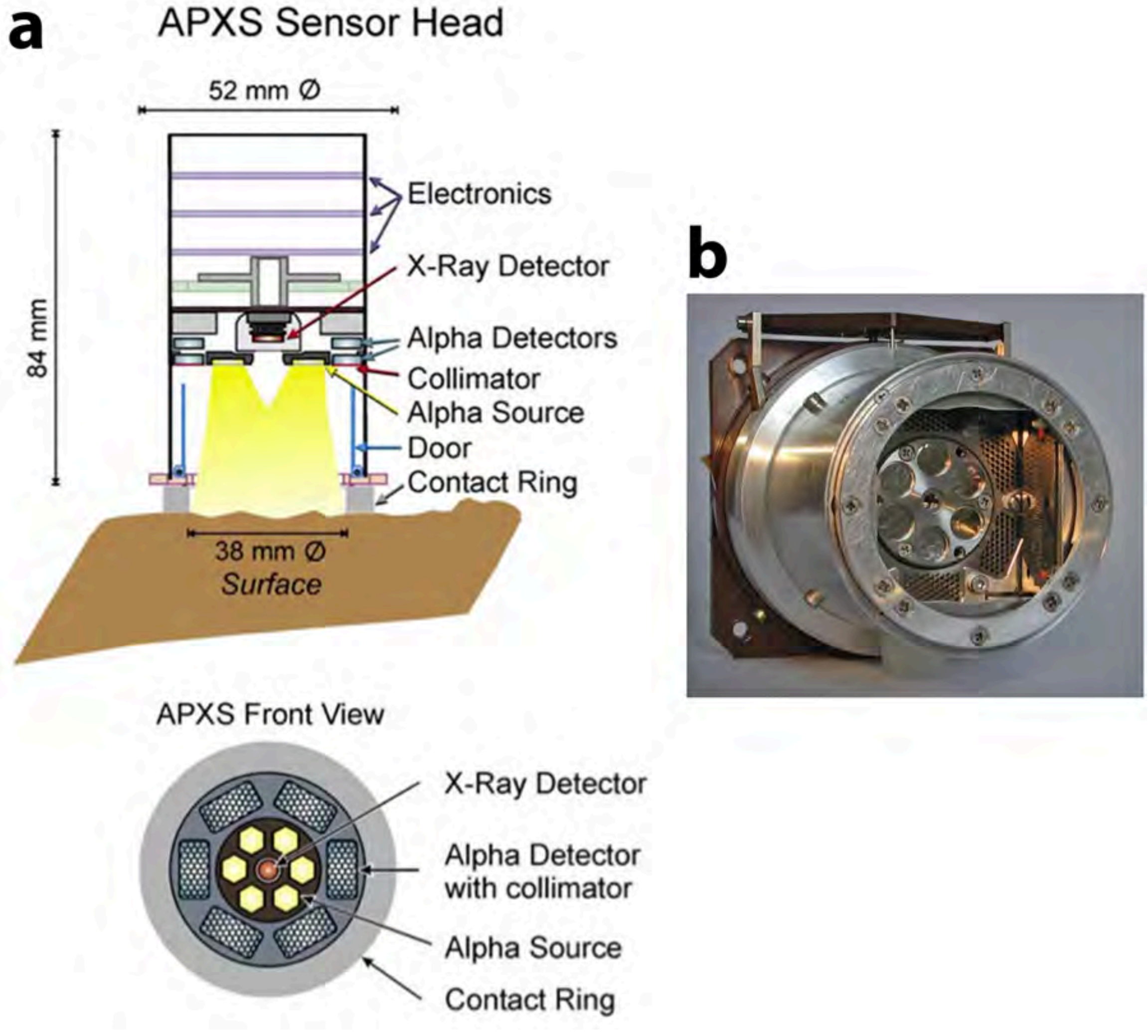

Figure 13. a) Schematic diagram and b) photograph of the MER Alpha Particle X-ray Spectrometer. Figures 4 and 5 from *Rieder et al.* [2003].

view is a 38 mm diameter circle, and the mean distance from the sample to the sources and detectors is ~30 mm.

The six ^{244}Cm alpha sources are covered with 2.5 μm thick Ti foil. The foil has two functions: to protect samples from the possibility of contamination by the source material, particles of which could otherwise be sputtered off by recoiling alpha particles; and to reduce the energy of the emitted alpha particles from 5.80 to 5.17 MeV to avoid a potential ~5.7 MeV ^{12}C(α, α')^{12}C resonance with atmospheric carbon, which would otherwise be a background for geological measurements. Consequently, the sensitivity for detecting carbon in geological samples was decreased as well [*Gellert et al.* 2006].

Six rectangular Si alpha detectors are arranged concentrically outside of the ring of alpha sources. The paths to the alpha detectors are collimated by 20 layers of stainless steel foils, etched with honeycomb patterns (see Figure 13). A second set of alpha detectors, set behind the sources and protected from their alpha emission, measure the background from cosmic rays and the high-energy gamma rays from decays of the APXS's ^{244}Cm and the Mössbauer Spectrometer's ^{57}Co sources.

X-rays are detected with a silicon drift detector, which has a 10 mm^2 active area and an energy resolution of ~160 eV at 5.9 keV, located in the central orifice of the ^{244}Cm source holder. The detector is sealed with a Be window [*Gellert et al.* 2006]. The X-ray field of view is defined by a collimator composed of one Zr aperture directly in front of the detector and another in the central orifice of the source holder (see Figure 13).

The X-ray and alpha modes always operate simultaneously. X-rays are detected in 512 channels ranging from ~850 eV to ~16 keV, and alpha particles are detected in 256 channels ranging up to ~6 MeV. When the APXS is operating, spectra and the temperatures of the electronics and sensor head are stored at 30 s intervals in a battery buffered, 32 kB SRAM, which can hold up to 12 spectra; the data are later transmitted to the rover computer for downlink.

2.2.4.3 Calibration

The flight instruments and their flight alpha sources were calibrated under Mars-like conditions (10 mbar CO_2 and a sensor temperature of ~ -35°C), using a set of oxide and metal standards, eight powdered geostandards, and three meteorites. The instrument was found to be insensitive to stray light. Additional calibration was conducted on a nearly identical, but non-flight, laboratory sensor head, obtaining spectra from ~100 additional standards and chemical compounds in order to gain a deeper theoretical understanding of the relationship between elemental composition and measured line intensities [*Gellert et al.* 2006]. A detailed description of pre- and post-launch calibration can be found in *Rieder et al.* [2003] and *Gellert et al.* [2006], respectively.

The sampling depths of the alpha and X-ray detection modes were investigated using a rock matrix sample of andesitic composition. Sampling depth was found to vary by mode and by element. For the alpha mode with a 0.5 MeV cutoff energy, maximum sampling depth ranged from 2 to 8 μm for C and Fe, respectively. In the X-ray mode, 95% of the total intensity was found to originate in layers ranging in thickness from 3.5 to 97 μm for Na and Fe, respectively.

After the rover landed on Mars, it was discovered that at “warm” temperatures, the capacitance of the cable that connects the APXS components on the IDD to the electronics in the WEB was degrading the signal. This led to operation of the instrument primarily at night, when temperatures were below -40°C [*Gellert et al.* 2006].

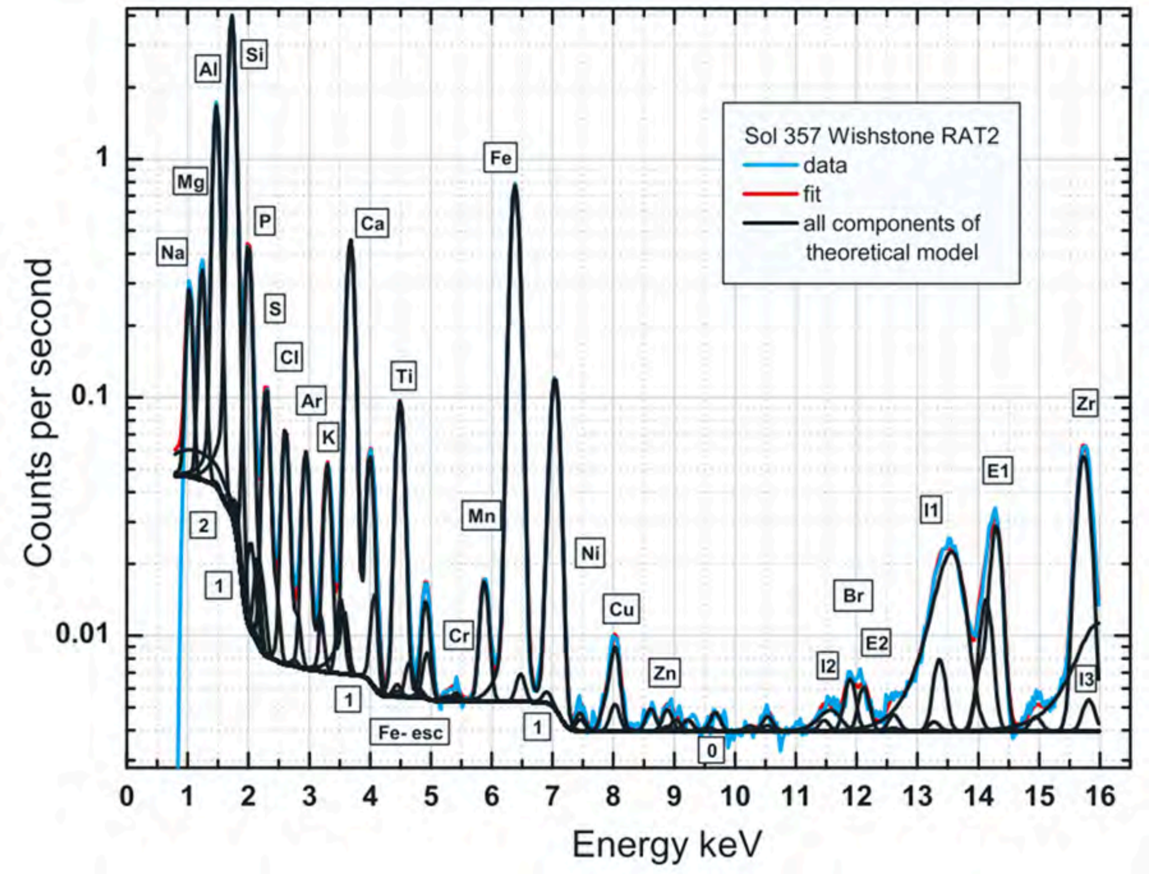

Figure 14. APXS X-ray spectrum of Wishstone Rock on Husband Hill, along with modeled spectral components. Figure 3 from *Gellert et al.* [2006].

The circumference of the APXS sensor head, 53 mm, is greater than that of the RAT's borehole, 45 mm, resulting in a difference in target-sensor distance for abraded and unabraded targets. The effect of the distance of the sensor head from the target was investigated in-flight by acquiring spectra from a rock target with standoff distances of 3.1, 6.1, 11.5, and 16.5 mm; the derived compositions did not vary significantly [*Gellert et al.* 2006].

2.2.4.4 Data Processing

Each element has unique peaks in an X-ray spectrum (see Figure 14). APXS elemental abundances are derived from the subspectral area of these peaks.

Radioactive sources on the IDD can contribute to the X-ray spectra measured by the APXS. The background due to the Mössbauer's main and reference ^{57}Co sources is mitigated with a 0.5 mm thick Ta shielding plates on both instruments. Other background sources arise from the materials composing the APXS sensor head itself: the Zr collimating structure, Cu in the mounting screw of the X-ray detector housing, and an elastically scattered signal from the Ti in the foils that cover the alpha sources. These backgrounds are accounted for during spectral deconvolution. Some measured spectra exhibit a peak position drift due to an imperfect temperature compensation gain; these are corrected by adjusting each spectrum to a common gain [*Gellert et al.* 2006].

All high-quality spectra for a given target are summed to increase the signal-to-noise ratio. The spectra are deconvolved with a non-linear least squares fitting algorithm, which outputs the peak areas of characteristic element lines along with statistical standard deviations. The peak areas are converted to element and then oxide weight percentages. The uncertainties reported for APXS elemental abundances are 2σ statistical uncertainties derived from peak area uncertainties, and do not include calibration uncertainties.

2.2.4.5 Spectral Libraries

Information in this section is from [*Gellert et al.* 2006] unless otherwise indicated.

Peak energy values from *Thompson et al.* [2001] are used in spectral deconvolution. The exception is the Ca Kα1 line, which has a peak in APXS spectra of 3.697 keV rather than the published 3.692 keV due to overlaps with backscattered Pu M lines; ^{240}Pu is the daughter particle of the ^{244}Cm decay. Up to five characteristic peaks per element are used, with ratios of the Kα and Kβ lines fixed to those measured during pre-flight calibration except for Fe, whose Kα and Kβ lines are strong and do not overlap with those of other elements. Peaks are assumed to be Gaussian.

Backgrounds included in the deconvolution include those described in Section 2.2.4.4, Compton scattering in the sample and detector, and elastic and inelastic scattering peaks of primary Pu X-ray radiation. The detector response function is also incorporated.

2.2.4.6 Data products

APXS data are archived in ASCII format as APXS Operations Experiment Data Records (EDRs), which include raw X-ray and alpha particle spectra; APXS X-ray spectra Science Reduced Data Records (RDRs), which are energy calibrated X-ray spectra; and APXS Oxide Abundance Data on the Planetary Data System (PDS) at http://pds-geosciences.wustl.edu/missions/mer/geo_mer_datasets.htm. Headers in all EDR and RDR files include a large amount of mission, instrument, telemetry, and data product metadata.

2.2.5 Mössbauer Spectrometer (MB)

The purpose of the MB is to provide quantitative information regarding iron-bearing phases in rock, soil and dust targets. Mössbauer spectrometers employ a source that emits gamma ray photons with energies similar to those in the target to be analyzed. The source is Doppler shifted in order to "scan" through and energies in the target nuclei. Data from the MB include the distribution of iron amongst its oxidation states (Fe^{2+}, Fe^{3+} and Fe^{6+}) and the identification and distribution of Fe amongst Fe-bearing phases, including silicates (*i.e.*, olivine, pyroxene), oxides (*i.e.*, magnetite, hematite, goethite), and other phases (*i.e.*, carbonates, sulfides, nanophase iron oxide) [*Morris et al.* 2006; *Klingelhöfer et al.* 2003]. While Fe Mössbauer spectroscopy has been used to examine extraterrestrial materials on Earth for decades, the MER mission was the first spacecraft mission to successfully fly a Mössbauer spectrometer [*Klingelhöfer et al.* 2003].

The Mössbauer effect is not unique to iron; however, in the following discussion, I refer to iron exclusively.

2.2.5.1 The Mössbauer effect

Information in this section is from *Wertheim* [1964] unless otherwise indicated.

The Mössbauer effect enables the identification of a mineral based on the electrical and magnetic field environments of an atomic nucleus within the crystal matrix.

Rudolf Ludwig Mössbauer discovered “recoilless nuclear resonance absorption”, the effect that now bears his name, while working on his doctoral thesis in 1957; he was awarded the Nobel Prize for this research in 1961. In “resonance absorption”, the amount of energy absorbed by a nucleus during excitation from a lower to a higher energy state is equal to the amount of energy emitted by that nucleus during relaxation from the higher to the lower state. The energy is absorbed and emitted in the form of a gamma ray photon. Due to the conservation of energy, a relaxing nucleus can be expected to recoil as it emits a gamma. If the nucleus in question is within an atom bound in a crystal lattice, and the recoil energy is less than that of the lattice’s phonon energy quantum, the atom cannot become displaced, nor can a lattice vibration be excited; the atom, and therefore the nucleus, cannot recoil. The Mössbauer effect arises from this “recoilless” case.

The energy spectrum of gamma ray photons emitted by relaxing nuclei will have a finite width. In the case of ^{57}Fe, the isotope analyzed by the MER MB instrument, recoilless emission can occur as a transition from the first excited state to the ground state, with an energy of 14.4129 keV. The excited nuclear state has a relatively long half-life of 98.3 nanoseconds [Bhat 1998], which corresponds to a theoretical linewidth of 3.3neV, though in practice, the linewidth is typically ~4.8neV [*Klingelhöfer et al.* 2003, *Qaim et al.* 1968]. This linewidth is smaller than the changes in nuclear energy levels induced by the atom’s oxidation state and the magnetic dipole and electric quadrupole interactions with the surrounding atoms and electrons in a crystal lattice: shifts in *nuclear* energy levels due to inclusion within a particular mineral crystal can be detected as a shift in the photon’s energy from the value it would have were it emitted from an isolated atom: 14.4 keV [*Wertheim* 1964, *Klingelhöfer et al.* 2003].

As the energy required to induce phonons can be provided by heat, the fraction of resonant absorptions resulting in recoilless emission decreases with temperature.

2.2.5.2 Observable Quantities

2.2.5.2.1 Isomer Shift (IS)

The isomer shift can be used to distinguish between oxidation (valence) states. It is an increase or decrease in the energy of the gamma emitted by the target nucleus, due to the electrostatic interaction between the nucleus and its atom’s electrons (see Figure 15). Isomers are nuclei with the same number of protons and neutrons, but which are in different energy states. The nuclear energy states are affected by the Coulomb interaction between the protons within the nucleus and the *s* orbital electrons, which have a non-zero probability of existing within the nucleus. The electron cloud density within the nucleus depends on the electrons’ orbital shell configuration, and therefore on the atom’s valence state.

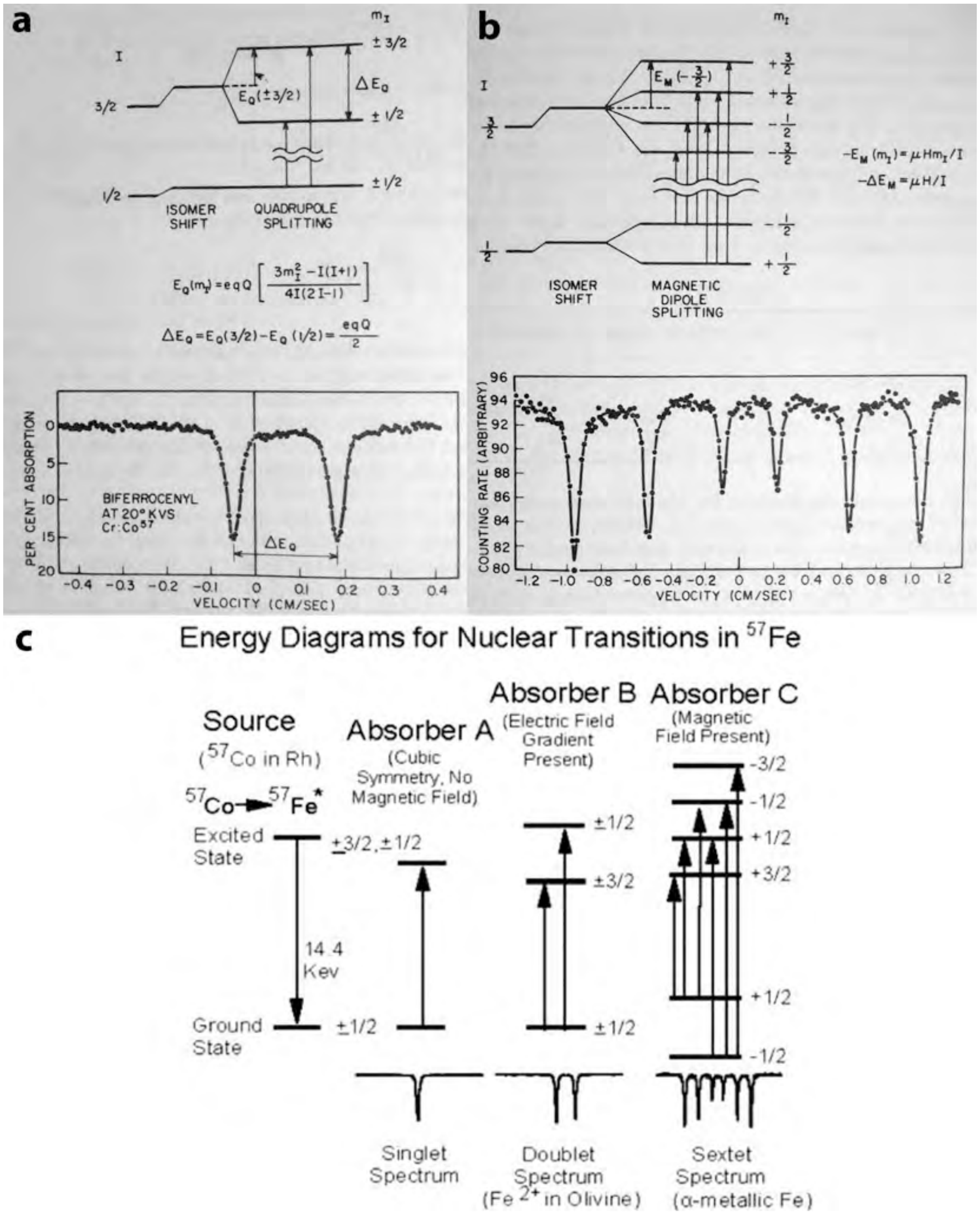

Figure 15. a) Effect of Isomer Shift and Quadrupole Splitting on nuclear energy levels (top) and the Mössbauer spectrum (bottom). Chapter VI, Figure 1 from *Wertheim* [1964]. b) Effect of Isomer Shift and Internal Magnetic Field Hyperfine Splitting on nuclear energy levels (top) and the Mössbauer spectrum (bottom). Chapter VII, Figure 1 from *Wertheim* [1964]. c) ^{57}Fe nuclear energy level diagrams (top) and Mössbauer spectra (bottom) for ^{57}Co source and three target absorbers (minerals) containing ^{57}Fe nuclei. Figure 1 from *Klingelhöfer et al.* (2003).

2.2.5.2.2 Quadrupole Coupling (QC)

Quadrupole coupling is affected by both the atom's valence state and the crystal's symmetry (*e.g.*, three-fold or four-fold symmetry, tetrahedral or octahedral coordination, etc.). It is a splitting of nuclear energy levels into doublets (see Figure 15) due to the interaction between a nucleus's quadrupole moment and the local electrostatic field gradient; the latter is created by both the electrons in its atom's incompletely filled shells, and the ions in the surrounding atoms in the crystal lattice [*Wertheim* 1964]. The ions contribute to the electrostatic field gradient if the crystal's symmetry is less than cubic. Quadrupole splitting does not distinguish between energy states whose magnetic quantum numbers have the same magnitude but opposite sign [*Wertheim* 1964].

2.2.5.2.3 Internal Magnetic Field Hyperfine Splitting (B_{hf})

The arrangement of the electrons in an atom's incompletely filled outer orbital shells gives rise to a magnetic field at the nucleus. The interaction between this field and the nuclear magnetic dipole moment results in hyperfine splitting of the nuclear energy states. The 14.4keV Mössbauer gamma is emitted when the nucleus transitions from the first excited state to the ground state. The magnetic quantum number $m_I = I, I - 1, \dots, -I$, where I is the nuclear spin quantum number (the vector sum of the nucleons' spins). The first excited state, for which I = 3/2, splits into four states, and the ground state, with I = 1/2, splits into a doublet. The combined hyperfine splitting of the two states results in a sextet of possible transitions (see Figure 15).

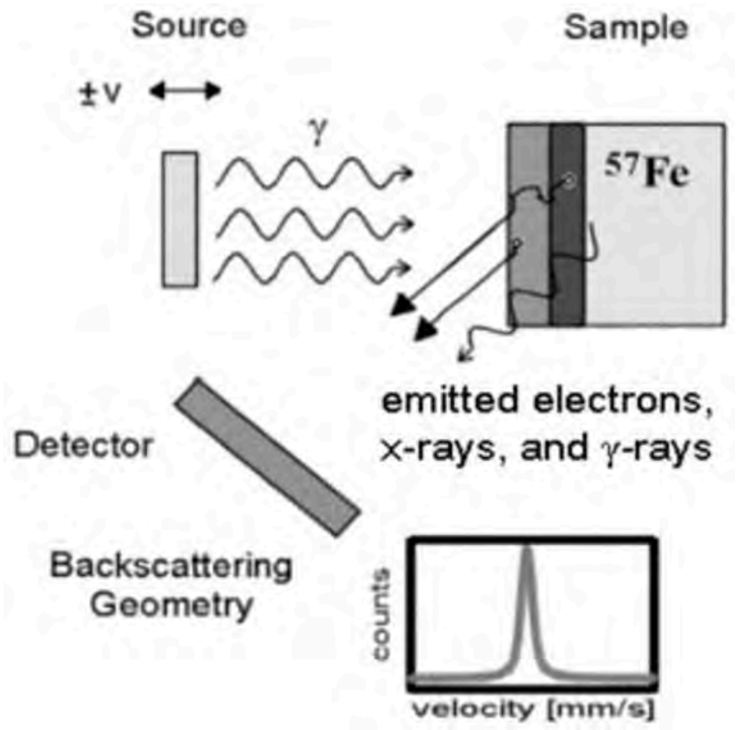

Figure 16. Schematic of a Mössbauer spectrometer operating in backscatter geometry. Adapted from Figure 2 of *Klingelhöfer et al.* [2003].

2.2.5.3 The MIMOS II Miniature Mössbauer Spectrometer

The information in this section is from *Klingelhöfer et al.* [2003] unless otherwise indicated.

The MIMOS II MB sensor head is mounted on the rover's IDD (see Figure 4); the electronics, including a dedicated CPU and 128 kB of volatile SRAM memory, are mounted in the Warm Electronics Box. MB can be used either with or without sample preparation by the RAT. The instrument is placed in contact with the target to be analyzed, and operates in backscatter geometry (see Figure 16). With this geometry, the instrument can make use of the 6.4 keV internal conversion X-rays for Mössbauer spectroscopy, in addition to the 14.4 keV gamma rays. Because nuclear states are temperature-dependent, MB spectral data is binned by temperature [*Morris et al.* 2006]. The widths of the 13 temperature intervals can be set by command from

Earth. The IDD maintains a preload, holding the sensor head firmly against the target, by means of a contact plate with a sensor, whose circular impression is often clearly visible on nonconsolidated targets such as soil and dust.

The instrument's resonant emission source is ^{57}Co in a Rh metal matrix. ^{57}Co decays to an excited nuclear state of ^{57}Fe, with a half-life of 271.8 days [*Haynes et al.* 2014-2015, Section 11, Table of the Isotopes]. The excited daughter nucleus emits the monochromatic gamma photons, which can be absorbed by ^{57}Fe nuclei within the target. ^{57}Fe has a natural abundance of ~2.2%. The MIMOS II source had an intensity of ~300mCi when it left Earth, and had degraded to ~30mCi by Sol 510 [*Morris et al.* 2006]. At this intensity, the instrument must acquire longer integrations than earlier in the mission, but the data quality remains high. The source is Doppler shifted by a transducer with a triangular waveform, which moves the source back and forth with a frequency of ~24Hz and a velocity range of ~±12mm/s [*Morris et al.* 2006]. The energy resolution is ~1.0-1.5 keV at room temperature and improves at lower temperatures; the efficiencies of 6.4 and 14.4 keV photons are nearly 100% and ~70%, respectively.

The detector is a set of four Si-PIN-diodes, each of which has a 10 x 10 mm^2 active area. It is shielded from the source by concentric tubes of brass, Ta and Pb. The shielding doubles as a collimator for the emitted gamma rays. The "beam size" of the emitted gammas is a compromise between the desire to maximize the sample size (and therefore minimize data acquisition time), and the need to minimize the angle between the moving source and the target. The Doppler shift between the source and the target is a function of the source velocity in the direction of the target nuclei; a wide angle of target illumination will result in a range of Doppler shifts at the locations of the absorbing nuclei. This effect, known as cosine smearing, not only broadens the Mössbauer peaks, it also shifts their centers outward, which affects the derived Mössbauer parameters and thus affects the modeled mineralogies. It was found that with a 5.6 mm collimator diameter, corresponding to a ~1.4 cm beam size on the target, MB can reliably resolve the components of a 1:1 mixture of hematite and maghemite, whose spectra strongly overlap.

The MB is instrumented with three temperature sensors: one on the electronics board in the Warm Electronics Box, one in the sensor head near the internal reference sample (see Section 2.2.5.4), and one on the contact plate to approximate the target temperature. The latter is used to divide the Mössbauer spectra into temperature intervals, which are assigned to different memory areas. All three temperatures are logged every 5 minutes during MB observations.

The MB sampling depth varies with target density (see Table 2); the instrument "sees" through surface dust coatings and samples the underlying rock.

2.2.5.4 Calibration

Information in this section is from *Klingelhöfer et al.* [2003] unless otherwise indicated.

Pre-flight calibration included a comparison of spectra of martian analog materials acquired by an engineering-model MIMOS II instrument and those acquired by a laboratory Mössbauer detector. The two sets of spectra coincided nearly exactly. Spectra were also acquired on reference rock slabs. A cosine smearing correction was found to be necessary for agreement between derived and literature values of the hyperfine splitting Mössbauer parameter. The isomer shift and quadrupole coupling parameters agreed within errors with and without the correction.

Knowledge of the relative velocity between the source and target is essential to properly analyze Mössbauer data. Pre-flight, the source drive systems were calibrated as a function of the

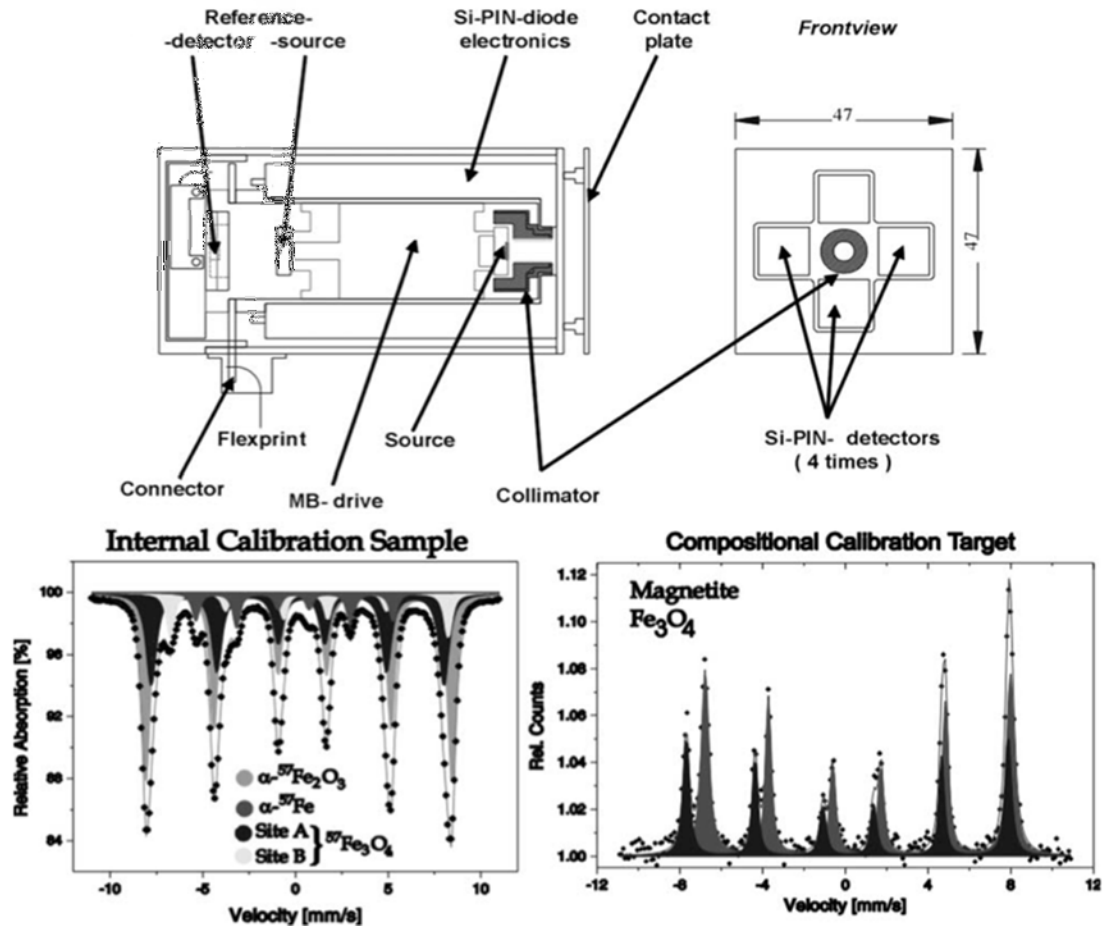

Figure 17. Schematic drawing of the MER Mössbauer spectrometer (top), and sample spectra (bottom). The internal calibration and compositional calibration spectra were acquired in transmission and backscatter geometry, respectively. Figure 4 from *Klingelhöfer et al.* [2006].

software velocity settings. In-flight calibration is conducted with a reference source, located on the same transducer as the main source, and a reference sample, in transmission geometry (see Figure 17). The reference sample is a mixture of α-Fe^0 (metallic iron) and α-Fe_2O_3 (hematite), which are 30% and 96% enriched in ^{57}Fe, respectively. Reference and target data are acquired simultaneously; the reference source and reference sample allow for in-flight calibration under the same conditions as target data acquisition. External sources of vibration, such as wind, can degrade the signal. The IDD is designed to maintain MB stability to less than 0.1 mm/sec [*Squyres et al.* 2003]. In addition, a prototype MIMOS II instrument was tested in the field; the resulting spectra did not exhibit detectable line broadening.

Each detector underwent pre-flight calibration with temperatures in the range 153 K – 293 K. Firmware parameters were calculated for each detector and each temperature interval. In-flight, the firmware can adjust these parameters during data acquisition to provide optimal detector performance for each temperature interval.

2.2.5.5 Data Processing

Information from this section is from *Klingelhöfer et al.* [2003] unless otherwise indicated.

The Mössbauer spectra are acquired as counts of photons referenced to the velocity of the source and the target (see Figure 16). Spectra are saved as 512 velocity channels, and binned in 13 temperature intervals.

Iron-bearing phases in the target area can be identified by modeling the measured spectrum as a linear combination of mineral signatures (IS, QC, and B_{hf}) from a spectral library. The spectral area of each mineral in a measured Mössbauer spectrum is proportional to the abundance of ^{57}Fe nuclei in that mineral in the sampling area times the mineral's fraction of recoilless transition. The distribution of iron across these phases can be assessed through their known recoilless fractions and modeled subspectral areas. The relative strengths of the sets of quadrupole coupling and hyperfine splitting lines for a given phase depend on the angle between the incident gammas and the principle axis of the electric field gradient and direction of magnetization, respectively.

Data from both energy modes were acquired and downlinked to Earth until Sol 461, at which time the rover was commanded to store data from the higher signal-to-noise 14.4 keV mode only [*Morris et al*. 2006]. *Morris et al.* [2006] explicitly state that their report is based on 14.4 keV spectra only.

2.2.5.6 Spectral Libraries

The information in this section is from *Morris et al.* [2006] unless otherwise indicated.

Because of the long history of Mössbauer spectroscopy on Earth, published lists of Mössbauer parameters (isomer shift, quadrupole coupling, and hyperfine splitting) exist for a large number of minerals (see Section 3.11 of *Morris et al.* [2006] for a list of such publications). Often, these do not include measurements at the temperatures for which MER MB data were acquired. However, because the MER MB source and target temperatures are typically within 10°C, published isomer shift parameter acquired at room temperature can be used to analyze MER data because in most cases, the source is at room temperature regardless of the temperature of the target. The quadrupole coupling parameters of paramagnetic doublets are not strongly temperature-dependent at martian diurnal temperatures, and while the quadrupole coupling and hyperfine splitting parameters of magnetic sextets are temperature-dependent, they have been measured at martian diurnal temperatures in studies of the magnetic properties of these phases.

2.2.5.7 Data products

MB data are archived on the Planetary Data System (PDS) at http://pds-geosciences.wustl.edu/missions/mer/geo_mer_datasets.htm in binary format as Mössbauer Operations Experiment Data Records (EDRs), which include pulse height analysis (PHA) spectra for each of the four sample and one reference detectors, Mössbauer spectra for each detector for each of the 13 temperature intervals, reference and sample temperatures, and engineering data; Mössbauer Summed Spectra Science Reduced Data Records (RDRs); and Mössbauer Relative Fe Abundance Data. Headers in all EDR and RDR files include a large amount of mission, instrument, telemetry, and data product metadata.

2.2.6 Rock Abrasion Tool (RAT)

Information in this section is from *Gorevan et al.* [2003] unless otherwise indicated.

Terrestrial field geologists carry rockhammers to expose fresh, unweathered, rock surfaces. The MER RAT is designed to prepare samples for analysis by the payload instruments by brushing away unconsolidated material from rock surfaces, and by abrading into rock targets.

On Sol 416, while abrading the Watchtower Rock target Joker, engineering data indicated that the RAT had worn through the diamond-impregnated resin on its bit. Brushing capability remained, but Spirit was unable to abrade subsequent targets.

2.2.6.1 Tool description

The RAT’s grinding “paddle wheel” consists of two 6.35 mm wide, slightly curved cutting heads arranged at opposite ends of a metal bar (see Figure 18). The cutting heads are composed of diamond-impregnated resin, which slowly ablates as the tool grinds into rock targets. As the wheel rotates around an axis at its center, the cutting heads trace out a circle with a diameter of 23.37 mm. In addition to rotating at ~3000 rotations per minute (RPM), the wheel revolves around the center of the RAT at a rate of 0-2 RPM based on the grind motor’s current reading, resulting in a circular grinding area with a 45 mm diameter. The tool abrades into the rocks in incremental steps that can be programmed from Earth. In order for the RAT to effectively grind into a surface, the IDD must provide a 10-100 N pre-load against the target. A Tooth brush, located on the IDD’s forearm, can be used to clean the grinding heads.

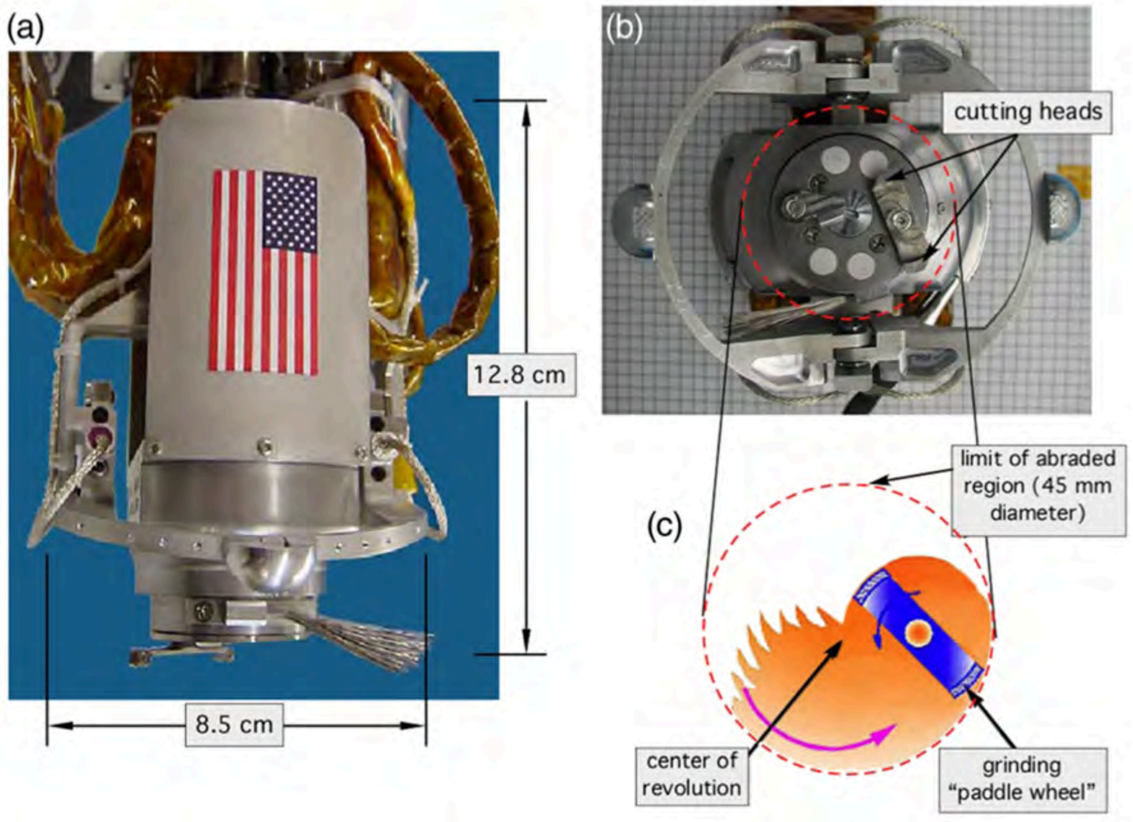

Figure 18. The MER Rock Abrasion Tool. a) Side view, showing the cable guard, which is made from aluminum recovered from the World Trade Center site following the attacks of September 11th, 2001. b) Front view, showing the cutting heads, brushed, and contact plate. The four grey circles are the RAT magnets (see Section2.2.7). c) Schematic diagram illustrating how the rotation and revolution of the grinding wheel result in a 45 mm diameter abraded region. Figure 1 from *Thompson et al.* [2013].

The RAT's brushing function includes a Rotate and a Revolve brush. The Rotate brush removes abraded material, often called RAT tailings, from the abraded region and deposits it on the perimeter of the hole. The Revolve brush pushes the material away from the edge of the RAT hole so that the Rotate brush deposits new material onto a relatively clean surface.

RAT Operations Experiment Data Records (EDRs), including motor positions, motor currents, contact switch states, temperature sensor values, bus voltage, software/algorithm states, and error bit fields, are archived on the Planetary Data System (PDS) at http://pds-geosciences.wustl.edu/missions/mer/geo_mer_datasets.htm

2.2.6.2 Specific Grind Energy (SGE) measurements

Information in this section is from *Thompson et al.* [2013].

In addition to its function as a sample preparation tool, telemetry from the RAT can be used to investigate the physical properties of rock targets. The current drawn by the grind motor varies with the hardness of the rock; soft rocks draw little current, and hard rocks draw more. The Specific Grind Energy (SGE) is the energy required by the RAT to abrade a given volume of rock, and is related to the compressive strength, mechanical behavior, hardness, and density of the rock. *Thompson et al.* [2013] show, through laboratory experiments involving an engineering flight spare of the RAT, that a linear relationship between SGE and compressive rock strength exists for rocks with strengths below ~150 MPa. They note that their sandstone sample fell below the SGE vs. rock strength trendline, which they attribute to the effectiveness of the RAT in dislodging cemented grains in this granular sample.

2.2.7 Magnetic Properties Experiments (MPE)

Information in this section is from *Madsen et al.* [2003] unless otherwise indicated.

Because Mars lacks plate tectonics, martian materials tend to be mafic (high in magnesium and iron), as opposed to the felsic (high in feldspar and silica) rocks that compose terrestrial continental crust. Previous landed missions have shown that the soil and dust are attracted to magnets, but they were unable to determine the ferrimagnetic phases. The purpose of the MER MPE is to analyze magnetic fines – including airfall dust, soil, and RAT tailings – with the full suite of the rover's scientific cameras and spectroscopic instruments. Establishing the composition(s) of the magnetic phase(s) in soil and airborne dust can constrain the formation

Table 8. Descriptions of magnets used in the Magnetic Properties Experiments. Most information is from *Madsen et al.* [2003]. Rock Abrasion Tool magnets size is from *Goetz et al.* [2008].

Magnet name	Location	Shape and size	Magnetic field strength	Purpose
Capture magnet	Front base of PMA	Central cylinder with r = 2.0 mm; 3 concentric rings, Outermost radius = 12.5 mm	B_{max} = 0.46 T $\nabla\|\boldsymbol{B}\|_{\mathrm{max}}$ = 550 T/m Magnetic pole orientation alternates with each ring	Strong magnet to attract dust particles Examination with IDD instruments
Filter magnet	Front base of PMA	Beveled, modified ellipse with a = 12.5mm b = 3.5mm	B_{max} = 0.2 T $\nabla\|\boldsymbol{B}\|_{\mathrm{max}}$ = 34 T/m	Attract dust particles with high magnetic susceptibility only Examination with IDD instruments
Sweep magnet	Near Pancam calibration target	Ring with r_{inner} = 2.0 mm r_{outer} = 4.5mm	B_{max} = 0.42 T $\nabla\|\boldsymbol{B}\|_{\mathrm{max}}$ = 450 T/m	Repel magnetic material to enable capture of non-magnetic atmospheric dust grains Examination with Pancam
Rock Abrasion Tool magnet	Mounted on RAT, behind the grinding tool and brush	Cylinders with r = 2.96 mm	*Type 1 (2 magnets)*: B_{max} = 0.28 T $\nabla\|\boldsymbol{B}\|_{\mathrm{max}}$ = 350 T/m Type 2 (1 magnet): B_{max} = 0.1 T $\nabla\|\boldsymbol{B}\|_{\mathrm{max}}$ = 120 T/m Type 3 (1 magnet): B_{max} = 0.07 T $\nabla\|\boldsymbol{B}\|_{\mathrm{max}}$ = 80 T/m	Capture magnetic minerals in abraded rock material Examination with Pancam

pathways of these particles, and therefore the history of water on Mars. All of the magnets are composed of Sm_2Co_{17} in an Al structure. Table 8 lists descriptions of the magnets; schematics of the magnets, the magnetic fields, and the magnetic field gradients are shown in Figure 19 and Figure 20.

This thesis does not make use of the Magnetic Properties Experiments.

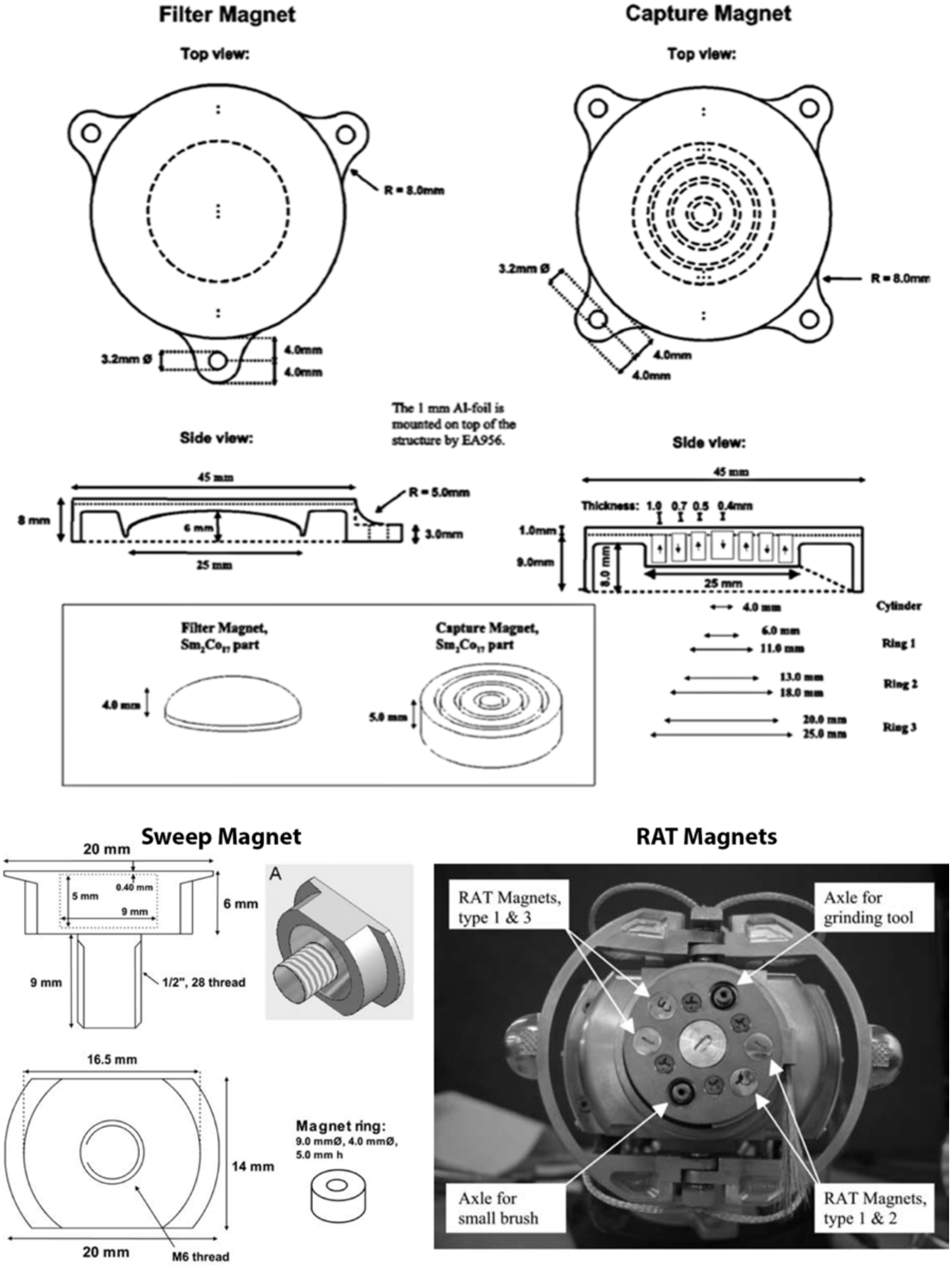

Figure 19. **The magnets of the Magnetic Properties Experiment. Figures 3, 6, and 8 from *Madsen et al.* [2003].**

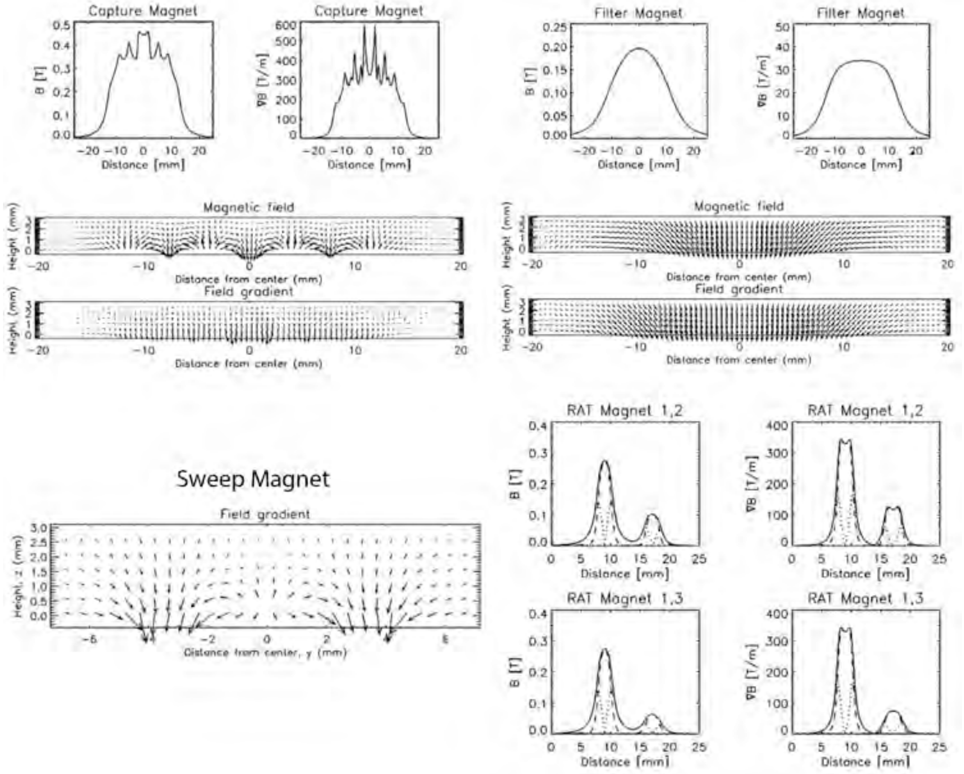

Figure 20. Magnetic fields and magnetic field gradients for the magnets of the Magnetic Properties Experiment. Figures 4, 5, 7, and 9 from *Madsen et al.* [2003].

2.2.8 Non-payload Engineering Cameras

The information in this section is from *Maki et al.* [2003] unless otherwise indicated.

Navcam and Hazcam were designed for engineering purposes rather than science, but are used for scientific studies. The engineering camera design and data formats were developed along side Pancam, and share many attributes. The 1024 x 2048 CCD described in Section 2.2.1.1 is used by all MER cameras.

2.2.8.1 Navigation Cameras (Navcam)

Navcam is a pair of mast-mounted cameras with a separation of 20 cm, located on the PMA between the Pancam cameras (see Figure 5). Unlike Pancam, Navcam has a single broadband visible filter, ranging from ~600 – 750 nm, and was not subjected to as rigorous a radiometric preflight calibration as Pancam. Stereo Navcam data are used by the rover team for terrain modeling for future drives, and by the rover itself for navigation, including hazard detection and avoidance, during autonomous drives. Navcam often captures mosaics, many of which cover 360°, to provide localization and context for Pancam and Mini-TES remote sensing.

The Navcam camera system is identical to that of Pancam. The optics differ: each Navcam camera has a 14.67 mm focal length, f/12, a 45° x 45° field of view (FOV), and an angular resolution of 0.82 mrad/pixel. Best focus is at 1.0 m, with a depth of field from 0.5 m to infinity.

2.2.8.2 Hazard Avoidance Cameras (Hazcam)

The rover has front and rear stereo Hazcams located on the rover body ~0.5 m above the ground, with a 10 cm baseline. The optics are significantly different from other MER cameras: f-theta fish-eye lenses with a 124° x 124° FOV, f/15, a focal length of 5.58 mm, and an angular

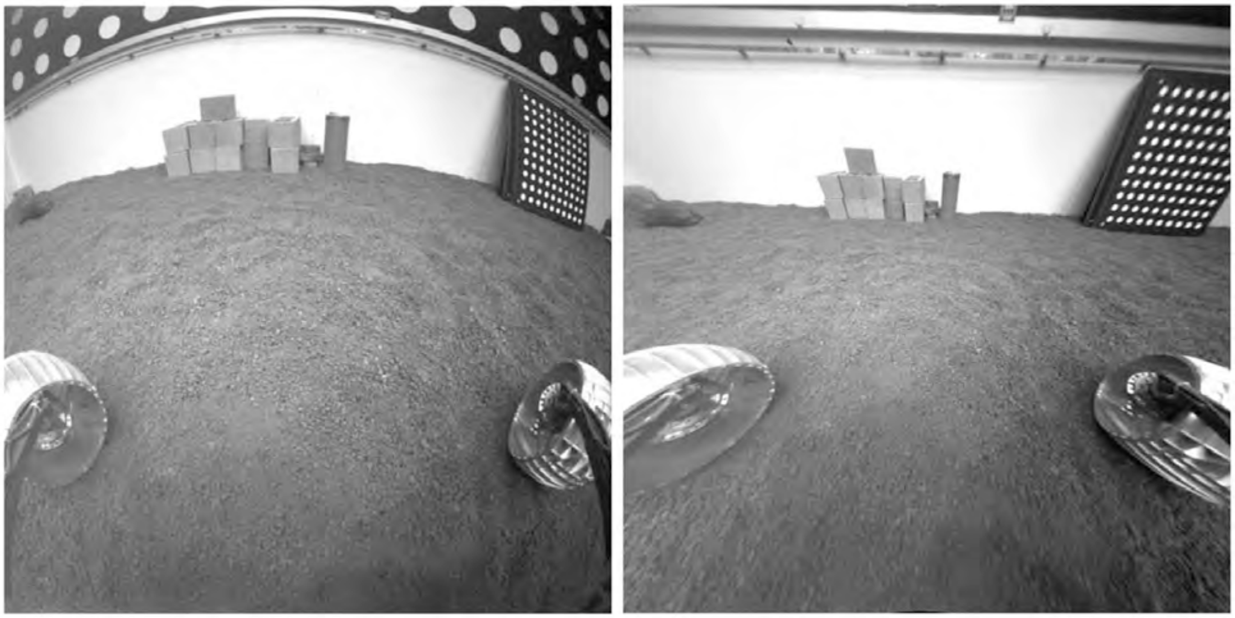

Figure 21. Front Hazcam image before (left) and after (right) linearization. The image was acquired in the MER Surface System Testbed (SSTB) "sandbox". Figures 18 (left) and 25 (right) from *Maki et al.* [2003].

resolution of 2.1mrad/pixel at the center of the image (see Figure 21). Like Navcam, each Hazcam camera has a single broadband visible filter.

Hazcam data are used to detect and model hazardous objects during autonomous navigation; to image the location, orientation, and potential and actual placement of the IDD; and to examine the terrain proximal to the rover, which cannot be seen by Navcam or Pancam.

2.3 Factors affecting data collection

Three significant constraints limit data collection within the MER mission. The first is that of rover memory: each rover has the equivalent of a 256MB USB stick. Another is power: the rovers are powered by solar arrays on the rover deck and fold-out panels (see Figure 4). Dust is ubiquitous on Mars, and ~2μm particles continuously fall out of atmospheric suspension, reducing the efficacy of the solar arrays. The third is downlink data volume. The rover does not transmit its data directly to Earth. Instead, she transmits data to an orbiter – typically Mars

Global Surveyor (MGS; now defunct), Mars Odyssey, or Mars Reconnaissance Orbiter (MRO) – and the orbiter transmits the data to the Deep Space Network of 35 m and 70 m radio antennas on Earth. Downlink data volume is controlled by the amount of time the rover can transmit to the orbiter, which passes over the rover twice per sol. When the rover's power is particularly high due to wind events that remove dust from the solar panels, it can downlink to the orbiter both during the day and at night, but throughout most of the mission, only daytime downlinks were possible. The volume of each downlink depends on the elevation of the orbiter's path with respect to the rover: a high elevation corresponds to a longer time above the horizon, and therefore a larger downlink. Typical daily downlink volumes are ~50-200 megabits (6-25 MB).

These constraints affect the work described in this thesis in that it was often not possible for the operations team to obtain and downlink all of the data one might wish for. In some cases, stereo data were not acquired; in others, the team opted for subframe images of selected targets rather than full-frame images that would have shown more context; in still others, some, but not all, of the in-situ instruments were used on a target. The team works well together, by consensus [*Vertesi* 2015], and the quantity and quality of the data returned are astounding. Aspects of the studies described in this thesis had been envisioned by the team while the rover examined the targets described, but team members were not working on these analyses. They obtained data with forethought. There are instances in which, had I been on the team and conducting this research at the time, I would have requested additional observations, but these will have to wait until other rovers or humans revisit the field site (see Appendix).

2.4 MER data and mission context

2.4.1 Obtaining MER science data

The data from the MER mission are archived primarily in the Planetary Data System (PDS), but data products are available online in several places. Some data are simple to find; others are more difficult. I have spent the past several years working with MER data, and I keep discovering it in new places. I hope that this compilation facilitates future researchers.

2.4.1.1 Planetary Data System (PDS)

The PDS is the official archive of data products from NASA planetary missions. In previous years, data were available on CD; now they are available online. The PDS is divided into nodes for Atmospheres, Geosciences, Imaging, Navigational & Ancillary Information (NAIF), Planetary Plasma Interactions (PPI), Planetary Rings, and Small Bodies. MER data are stored in the Atmospheres, Geosciences, Imaging, and NAIF nodes, and are available at:

http://pds-atmospheres.nmsu.edu/cgi-bin/getdir.pl?dir=INDEX&volume=merimu_1001
http://pds-atmospheres.nmsu.edu/cgi-bin/getdir.pl?dir=INDEX&volume=merimu_2001
http://pds-geosciences.wustl.edu/missions/mer/geo_mer_datasets.htm
http://img.pds.nasa.gov/portal/mer_mission.html
http://naif.jpl.nasa.gov/pub/naif/MER/kernels/

2.4.1.2 MER Analyst's Notebook

NASA's PDS Geosciences Node at Washington University in St. Louis produces the Analyst's Notebook series of websites; they are currently available for the Spirit, Opportunity, Curiosity, Phoenix, LCROSS, and Apollo (11, 12, 14, 15, 16, and 17) missions. The "notebooks" are graphical user interfaces to PDS data, and are designed for use by the scientific community. Data are organized in several, meaningful ways. The following list refers to the MER Analyst's Notebook specifically:

- Mission Summaries, which are historical overviews that briefly list each sol’s activities
- Sol Summaries, which list:
    - An Overview of that sol in the context of the mission
    - Every Data Product acquired on that sol, including derived data products and Mini-TES context images, easily available for viewing or download
    - Documents, including Mission Manager and Science Operations Working Group (SOWG) Documentarian reports, written by team members for mission planning purposes. These, particularly the Documentarian reports, provide context for the data products.
    - The Science Team Activity Plan, which lists the planned sequence of activities and observations for that sol and includes links to the data products
    - Mosaics, from Navcam, Pancam and MI; Pancam and Navcam mosaics are often available with multiple projections
    - Special Products, including approximately true- and false-color Pancam mosaics and MI merged focal images
- A Search function, with options for searching by mission clock time, rover location, instrument, command sequence, image “eye” and filter, mosaics, special products, product type, and product ID
- Map of the rover’s traverse, showing the rover’s location on each sol, with links to that sol’s data
- Resources, with links to Additional Data Sets, Mission and Instrument Data Set Documents, Coordinate Systems used in the mission, Software for viewing and manipulating the data, a Reference List of special issues of scientific journals focused on the MER mission, and links to Other Resources such as the PDS and other NASA websites

Users can create free accounts in order to bookmark items, place them in a cart to download a group of data products rather than downloading each product individually, and to save user settings. Full access to the Analyst's Notebook is available whether or not the user creates an account.

The MER Analyst's Notebook considerably facilitated the work described in this thesis. In addition to providing an excellent resource for locating and obtaining MER data, Thomas Stein, who maintains the site, is incredibly responsive to comments and suggestions regarding functionality. If something doesn't work the way you think it should, don't hesitate to use the "Contact Us" link at the bottom of the page or the "Email Us" link in the Help menu, or send an email to an@wunder.wustl.edu.

2.4.1.3 Pancam website

Processed Pancam images can be found on the Pancam website:
http://marswatch.astro.cornell.edu/pancam_instrument/images.html
This is a beautiful and easy way to browse for approximate true color and false color single-frame images, 360° Panoramas, Small Panoramas and Mosaics, and "Team Favorites". Many mosaics and panoramas are available in approximate true color and false color, and as anaglyphs. Visitors to the website can also read about Pancam Research and Development. Special projects, including nighttime observations (rover-based astronomy) and images and animations of Phobos and Deimos transiting the Sun (Martian solar eclipses), are available at http://marswatch.astro.cornell.edu/pancam_instrument/projects.html.
Many of the color images used within figures in this thesis were downloaded from this site.

2.4.1.4 USGS

The United States Geological Survey surveys more than rocks within the U.S. borders. The USGS lab in Flagstaff, AZ, includes an Astrogeology Science Center, and many USGS geologists work "on" Mars, including MER team members. MI/Pancam color merged images can be found on the USGS website, at:

http://astrogeology.usgs.gov/maps/mars-mer-mi-merged-products

2.4.1.5 Mars Exploration Rovers Image and Video Galleries

All MER images are uploaded to the World Wide Web upon downlink from Mars. Every raw image acquired by the rovers' Front and Rear Hazcam; Navcam; Pancam; MI; and Entry, Descent, and Landing cameras can be viewed and downloaded from http://mars.jpl.nasa.gov/mer/gallery/all/spirit.html (Spirit) and http://mars.jpl.nasa.gov/mer/gallery/all/opportunity.html (Opportunity). Selected press release images, raw images, panoramas, 3-D images (anaglyphs), "special effects" images, images of the spacecraft, Mars artwork, and images of the landing site are available at http://mars.jpl.nasa.gov/mer/gallery/images.html. Videos, including rendered animations, team member reflections and narrations, flyover animations based on 3D orbiter data, and animations assembled from rover images, are available at http://mars.jpl.nasa.gov/mer/gallery/video/.

2.4.1.6 The Exploratorium

The Exploratorium, "a museum of science, art, and human perception" in San Francisco, has an extensive website about the Mars Exploration Rovers. Raw image data are uploaded daily, and are available on this site:

http://www.exploratorium.edu/mars/spiritopp.php

2.4.2 Mission Context

2.4.2.1 Google Mars

Geologists love Google Earth. It is an excellent means of examining the geography, geomorphology, and topography of our planet, at a range of scales. The program is not limited to Earth: it can also be used to explore Mars, the Moon, and the night sky. The user can view Mars through multiple orbital datasets, including visible imagery, daytime and nighttime infrared imagery, and colorized topography. The program also includes data from rovers and landers, including rover traverse paths and mosaics. It is an excellent way to explore the geomorphology in the vicinity of a rover's landing site, and to view 360° Pancam panoramas.

The online http://www.google.com/mars/ is simpler, and primarily useful for viewing orbital image and topography data at large scales.

2.4.2.2 Unmanned Spaceflight forum

http://unmannedspaceflight.com/ is an online forum started by Doug Ellison in 2004. The members of the forum are primarily lay enthusiasts, though MER team members also contribute to the site. Posts on the MER fora include discussions about the mission, (often spectacular) images and animations processed from MER data, original images and animations, and occasional poetry.

2.4.2.3 *Roving Mars*

This book was written by Steve Squyres, the Principle Investigator of the Mars Exploration Rover mission (and my PhD advisor). It chronicles the trials, tribulations and wonders of robotic spaceflight, from rejected mission proposals through the first several months of the rovers' explorations on Mars. This book, and the IMAX film of the same name, provide an excellent behind-the-scenes view of the mission.
Squyres, S. (2005), *Roving Mars,* Hyperion, New York, ISBN 9781401301491.

2.4.2.4 Ethnography of the Mars Exploration Rover Team

Janet Vertesi, now an Assistant Professor in the Sociology Department at Princeton University, works in the fields of Science and Technology Studies (STS) and Human-Computer Interaction (HCI). She wrote her PhD dissertation on the Mars Exploration Rover team. The dissertation, *Seeing Like a Rover: Images in Interaction on the Mars Exploration Rover Mission*, is available online at:

http://ecommons.library.cornell.edu/handle/1813/13524

This work has recently been published as a book by the University of Chicago Press:

Vertesi, J. (2015), *Seeing Like a Rover: How Robots, Teams, and Images Craft Knowledge of Mars*, University of Chicago Press, Chicago, IL, ISBN 9780226155968 (cloth), 9780226156019 (E-book).

Vertesi describes research on the MER team (and on other spacecraft mission teams) on her website:

http://janet.vertesi.com/projects/seeing-rover

and http://janet.vertesi.com/projects/social-life-spacecraft

She presented a public talk at the Exploratorium, describing how the MER scientists learned how to “See like a Rover”, which can be viewed online at

http://www.exploratorium.edu/tv/?project=2&program=1386&type=clip

BIBLIOGRAPHY

Alexander, D. A., Deen, R. G., Andres, P. M., et al. (2006), Processing of Mars Exploration Rover imagery for science and operations planning, *J. Geophys. Res., 111*, E02S02, doi:10.1029/2005JE002462.

Arvidson, R. E., Squyres, S. W., Anderson, R. C., et al. (2006), Overview of the Spirit Mars Exploration Rover Mission to Gusev Crater: Landing site to Backstay Rock in the Columbia Hills, *J. Geophys. Res., 111*(E2), E02S01, doi:10.1029/2005JE002499.

Arvidson, R. E., Ruff, S. W., Morris, R. V., et al. (2008). Spirit Mars Rover Mission to the Columbia Hills, Gusev Crater: Mission overview and selected results from the Cumberland Ridge to Home Plate. *J. Geophys. Res.*, *113*(E12), E12S33, doi:10.1029/2008JE003183.

Bell, J. F., III, Squyres, S. W., Herkenhoff, K. E., et al. (2003), Mars Exploration Rover Athena Panoramic Camera (Pancam) investigation, *J. Geophys. Res., 108*(E12)*,* 8063, doi:10.1029/2003JE002070.

Bell, J. F., III, Joseph, J., Sohl-Dickstein, J. N., et al. (2006), In-flight calibration and performance of the Mars Exploration Rover Panoramic Camera (Pancam) instruments, *J. Geophys. Res.*, *111*(E2), E02S03, doi:10.1029/2005JE002444.

Bhat, M. R. (1998). Nuclear Data Sheets for A = 57, Nuclear Data Sheets, 85, 415, doi: 10.1006/ndsh.1998.0021. Available online at http://www.nndc.bnl.gov/chart/getdataset.jsp?nucleus=57FE&unc=nds.

Burns, R. G. (1993), Origin of electronic spectra of minerals in the visible to near-infrared region, in *Remote Geochemical Analysis: Elemental and Mineralogical Compostion*, Topics in Remote Sensing 4, edited by C. M. Pieters and P. A. Englert, pp. 3-29, Cambridge University Press, New York, NY.

Cabrol, N. A., Grin, E. A., Carr, M. H., et al. (2003). Exploring Gusev Crater with Spirit: Review of science objectives and testable hypotheses, *J. Geophys. Res.*, *108*(E12), 8076, doi:10.1029/2002JE002026.

Cabrol, N. A., Farmer, J. D., Grin, E. A., et al. (2006), Aqueous processes at Gusev Crater inferred from physical properties of rocks and soils along the Spirit traverse, *J. Geophys. Res., 111*, E02S20, doi:10.1029/2005JE002490.

Callas, J. L. (2011), A Job Well Exceeded, email to the Mars Exploration Rover Team.

Carr, M. H. (2007), *The Surface of Mars*, Cambridge Planetary Science Series, Cambridge University Press, New York, doi: 10.1017/CBO9780511536007.

Che, C., and Glotch, T. D. (2012). The effect of high temperatures on the mid-to-far-infrared emission and near-infrared reflectance spectra of phyllosilicates and natural zeolites: Implications for martian exploration. *Icarus*, *218*(1), 585–601, doi:10.1016/j.icarus.2012.01.005.

Christensen, P. R., Anderson, D. L., Chase, S. C., et al. (1992), Thermal emission spectrometer experiment: Mars Observer mission. *J. Geophys. Res.*, *97*(E5), 7719–16, doi:10.1029/92JE00453.

Christensen, P. R., Bandfield, J. L., Hamilton, V. E., et al. (2000), A thermal emission spectral library of rock-forming minerals. *J. Geophys. Res.*, *105*(E4), 9735–9739, doi:10.1029/1998JE000624.

Christensen, P. R., Mehall, G. L., Silverman, S. H., et al. (2003), Miniature Thermal Emission Spectrometer for the Mars Exploration Rovers, *J. of Geophys. Res.*, *108*(E12), 8064, doi:10.1029/2003JE002117.

Christensen, P. R., Ruff, S. W., Fergason, R. L., et al. (2004), Initial Results from the Mini-TES Experiment in Gusev Crater from the Spirit Rover. *Science*, *305*(5685), 837–842, doi:10.1126/science.1100564.

Clark, B. C., III, Arvidson, R. E., Gellert, R., et al. (2007), Evidence for montmorillonite or its compositional equivalent in Columbia Hills, Mars, *J. Geophys. Res., 112*, E06S01, doi:10.1029/2006JE002756.

Cole, S. B., Knudson, A. T., Rice, M. S., and Squyres, S. W. (2009), Spectral variation and alteration across the Cumberland Ridge outcrops, Columbia Hills, Mars, Abstract P13A-1249 presented at 2009 Fall Meeting, AGU, San Francisco, CA, 14-18 December 2009.

Cole, S. B., and Squyres, S. W. (2014), Field Guide to Husband Hill, Gusev Crater, *Eighth International Conference on Mars*, Abstract #1031.

Cole, S. B., Herkenhoff, K. E., Yingst, R. A., and Squyres, S. W. (2014), Similar microtextures in Watchtower and Comanche Class rocks at Gusev Crater, *LPSC XLVI*, Abstract #1652.

Cornell, R. M. and Schwertmann, U. (2003), *The iron oxides: Structure, properties, reactions, occurences and uses*, 2nd Ed., Wiley-VCH, Weinheim, doi: 10.1002/3527602097.

Crisp, J. A., Adler, M., Matijevic, J. R., et al. (2003), Mars Exploration Rover mission, J. Geophys. Res., 108(E12), 8061, doi:10.1029/2002JE002038.

Crumpler, L. S., Arvidson, R. E., Squyres, S. W., et al. (2011), Field reconnaissance geologic mapping of the Columbia Hills, Mars, based on Mars Exploration Rover Spirit and MRO HiRISE observations, *J. Geophys. Res., 116*, E00F24, doi:10.1029/2010JE003749.

Elachi, C., (1987), *Introduction to the physics and techniques of remote sensing*, Wiley Series in Remote Sensing, John Wiley & Sons, New York, NY.

Evans, D. L., and Adams, J. B. (1980), Amorphous gels as possible analogs to Martian weathering products. *LPSC XI Proceedings*, 757–763. Retrieved from adsabs.harvard.edu/abs/1980LPSC...11..757E

Feely, K. C., and Christensen, P. R. (1999), Quantitative compositional analysis using thermal emission spectroscopy: Application to igneous and metamorphic rocks. *J. Geophys. Res.*, *104*(E10), 24195–16, doi:10.1029/1999JE001034.

Fergason, R. L., Christensen, P. R., Bell, J. F., III, et al. (2006), Physical properties of the Mars Exploration Rover landing sites as inferred from Mini-TES–derived thermal inertia, *J. Geophys. Res.*, *111*(E2), E02S21, doi:10.1029/2005JE002583.

Francis, D. (2011), Columbia Hills – An exhumed layered igneous intrusion on Mars?, *EPSL 310*, 59-64, doi:10.1016/j.epsl.2011.08.003.

Gellert, R., Rieder, R., Brückner, J., et al. (2006), Alpha Particle X-Ray Spectrometer (APXS): Results from Gusev crater and calibration report, *J. Geophys. Res., 111*, E02S05, doi:10.1029/2005JE002555.

Glotch, T. D., and Bandfield, J. L. (2006), Determination and interpretation of surface and atmospheric Miniature Thermal Emission Spectrometer spectral end-members at the Meridiani Planum landing site, *J. Geophys. Res.*, *111*(E12), E12S06, doi:10.1029/2005JE002671.

Glotch, T. D., Bandfield, J. L., Christensen, P. R., et al. (2006), Mineralogy of the light-toned outcrop at Meridiani Planum as seen by the Miniature Thermal Emission Spectrometer and implications for its formation, *J. Geophys. Res.*, *111*(E12), E12S03, doi:10.1029/2005JE002672.

Goetz, W., Leer, K., Gunnlaugsson, H. P., et al. (2008), Search for magnetic minerals in Martian rocks: Overview of the Rock Abrasion Tool (RAT) magnet investigation on Spirit and Opportunity, *J. Geophys. Res.*, *113*(E5), E05S90, doi:10.1029/2006JE002819.

Golombek, M. P., Grant, J. A., Parker, T. J., et al. (2003). Selection of the Mars Exploration Rover landing sites. *J. of Geophys. Res.*, *108*(E12), 8072, doi:10.1029/2003JE002074.

Gorevan, S. P., Myrick, T., Davis, K., et al. (2003), Rock Abrasion Tool: Mars Exploration Rover mission. *J. Geophys. Res.*, *108*(E12), 8068, doi:10.1029/2003JE002061.

Grant, J. A., Arvidson, R., Bell, J. F., III, et al. (2004), Surficial Deposits at Gusev Crater Along Spirit Rover Traverses, *Science*, *305*(5685), 807–810, doi:10.1126/science.1099849.

Grant, J. A., Wilson, S. A., Ruff, S. W., et al. (2006), Distribution of rocks on the Gusev Plains and on Husband Hill, Mars. *Geophys. Res. Lett.*, *33*(16), L16202, doi:10.1029/2006GL026964.

Greeley, R., Arvidson, R. E., Bartlett, P. W., et al. (2006), Gusev crater: Wind-related features and processes observed by the Mars Exploration Rover Spirit, *J. Geophys. Res., 111*, E02S09, doi:10.1029/2005JE002491.

Hamilton, V. E., Christensen, P. R., and McSween, H. Y. (1997), Determination of Martian meteorite lithologies and mineralogies using vibrational spectroscopy, *J. Geophys. Res.*, *102*(E11), 25593–25603, doi:10.1029/97JE01874.

Hamilton, V. E., and Christensen, P. R. (2000), Determining the modal mineralogy of mafic and ultramafic igneous rocks using thermal emission spectroscopy, *J. Geophys. Res.*, *105*(E4), 9717–9733, doi:10.1029/1999JE001113.

Hamilton, V. E., and Ruff, S. W. (2012). Distribution and characteristics of Adirondack-class basalt as observed by Mini-TES in Gusev crater, Mars and its possible volcanic source. *Icarus*, *218*(2), 917–949, doi:10.1016/j.icarus.2012.01.011.

Hayes, A. G., Grotzinger, J. P., Edgar, L. A., et al. (2011), Reconstruction of eolian bed forms and paleocurrents from cross-bedded strata at Victoria Crater, Meridiani Planum, Mars, *J. Geophys. Res.*, *116*, E00F21, doi:10.1029/2010JE003688.

Haynes, W. M. (Editor-in-Chief) (2014-2015), *CRC Handbook of Chemistry and Physics*, 95th ed. [Online], CRC Press, http://www.hbcpnetbase.com/ (accessed October 17, 2014).

Herkenhoff, K. E., Squyres, S. W., Bell, J. F., III, et al. (2003), Athena Microscopic Imager investigation, *J. Geophys. Res.*, *108*(E12), 8065, doi:10.1029/2003JE002076.

Herkenhoff, K. E., Squyres, S. W., Anderson, R., et al. (2006), Overview of the Microscopic Imager Investigation during Spirit's first 450 sols in Gusev crater, *J. Geophys. Res., 111*, E02S04, doi:10.1029/2005JE002574.

Hurowitz, J. A., McLennan, S. M., McSween, H. Y., et al. (2006), Mixing relationships and the effects of secondary alteration in the Wishstone and Watchtower Classes of Husband Hill, Gusev Crater, Mars, *J. Geophys. Res., 111*, E12S14, doi:10.1029/2006JE002795.

van Kan Parker, M., Zegers, T., Kneissl, T., et al. (2010), 3D structure of the Gusev Crater region. *Earth and Planetary Science Letters*, *294*(3-4), 411–423, doi:10.1016/j.epsl.2010.01.013.

Klingelhöfer, G., Morris, R. V., Bernhardt, B., et al. (2003), Athena MIMOS II Mössbauer spectrometer investigation, *J. Geophys. Res., 108*(E12), 8067, doi:10.1029/2003JE002138.

Knechtel, M. M., and Patterson, S. H., (1962) Bentonite deposits of the Northern Black Hills District, Wyoming, Montana, and South Dakota, U.S. Geol. Survey Bull. 1082-M. Available online at http://pubs.er.usgs.gov/publication/b1082M.

Lane, M. D., Bishop, J. L., Dyar, M. D., et al. (2008), Mineralogy of the Paso Robles soils on Mars. *American Mineralogist*, *93*(5-6), 728–739, doi:10.2138/am.2008.2757.

Le Bas, M. J. (1981), Carbonatite magmas. *Miner. Mag.*, *44*, 133–140.

Le Bas, M. J., Le Maitre, R. W., Streckeisen, A., and Zanettin, B. (1986), A Chemical Classification of Volcanic Rocks Based on the Total Alkali-Silica Diagram. *J. Petrol.*, *27*(3), 745–750, doi:10.1093/petrology/27.3.745

Le Maitre R.W. (2002) *Igneous rocks : IUGS classification and glossary of terms : Recommendations of the International Union of Geological Sciences Subcommission on the Systematics of igneous rocks*, *2nd ed*. Cambridge University Press, Cambridge.

Lewis, K. W., Oharonson, O., Grotzinger, J. P., et al (2008), Structure and stratigraphy of Home Plate from the Spirit Mars Exploration Rover, *J. Geophys. Res., 113*, E12S36, doi:10.1029/2007JE003025.

Lorre, J. and Deen, B. (1999) VICAR-marscorr, NASA/JPL; http://www-mipl.jpl.nasa.gov/external/vicar.html.

Madsen, M. B., Bertelsen, P., Goetz, W., et al. (2003), Magnetic Properties Experiments on the Mars Exploration Rover mission, *J. Geophys. Res.*, *108*(E12), 8069, doi:10.1029/2002JE002029.

Maki, J. N., Bell, J. F., III, Herkenhoff, K. E., et al. (2003), Mars Exploration Rover Engineering Cameras, *J. Geophys. Res., 108*(E12), 8071, doi:10.1029/2003JE002077.

McCoy, T. J., Sims, M., Schmidt, M. E., et al. (2008), Structure, stratigraphy, and origin of Husband Hill, Columbia Hills, Gusev Crater, Mars, *J. Geophys. Res., 113,* E06S03, doi:10.1029/2007JE003041.

McEwen, A. S., Eliason, E. M., Bergstrom, J. W., et al. (2007), Mars Reconnaissance Orbiter's High Resolution Imaging Science Experiment (HiRISE), *J. Geophys. Res.*, *112*, E05S02, doi:10.1029/2005JE002605.

McSween, H. Y., Arvidson, R. E., Bell, J. F., III, et al. (2004), Basaltic rocks analyzed by the Spirit Rover in Gusev Crater, *Science, 305*, 842-845, doi:10.1126/science.3050842.

McSween, H. Y., Ruff, S. W., Morris, R. V., et al. (2006), Alkaline volcanic rocks from the Columbia Hills, Gusev crater, Mars, *J. Geophys. Res., 111*, E09S91, doi:10.1029/2006JE002698.

McSween, H. Y., Ruff, S. W., Morris, R. V., et al. (2008), Mineralogy of volcanic rocks in Gusev Crater, Mars: Reconciling Mössbauer, Alpha Particle X-Ray Spectrometer, and Miniature Thermal Emission Spectrometer spectra, *J. Geophys. Res., 113*, E06S04, doi:10.1029/2007JE002970.

Ming, D. W., Mittlefehldt, D. W., Morris, R. V., et al. (2006), Geochemical and mineralogical indicators for aqueous processes in the Columbia Hills of Gusev crater, Mars, *J. Geophys. Res., 111*, E02S12, doi:10.1029/2005JE002560.

Ming, D. W., Gellert, R., Morris, R. V., et al. (2008), Geochemical properties of rocks and soils in Gusev Crater, Mars: Results of the Alpha Particle X-Ray Spectrometer from Cumberland Ridge to Home Plate, *J. Geophys. Res., 113*, E12S39, doi:10.1029/2008JE003195.

Mittlefehldt, D. W., Gellert, R., McCoy, T., et al. (2006), Possible Ni-rich mafic-ultramafic magmatic sequence in the Columbia Hills: Evidence from the Spirit Rover, *Lunar Planet. Sci. [CD-ROM], XXXVII*, Abstract 1505.

Morris, R. V., Klingelhöfer, G., Schröder, C., et al. (2006), Mössbauer mineralogy of rock, soil, and dust at Gusev crater, Mars: Spirit's journey through weakly altered olivine basalt on the plains and pervasively altered basalt in the Columbia Hills, *J. Geophys. Res., 111*, E02S13, doi:10.1029/2005JE002584.

Morris, R. V., Klingelhöfer, G., Schröder, C., et al. (2008), Iron mineralogy and aqueous alteration from Husband Hill through Home Plate at Gusev Crater, Mars: Results from the Mössbauer instrument on the Spirit Mars Exploration Rover, *J. Geophys. Res., 113*, E12S42, doi:10.1029/2008JE003201.

Morris, R.V., Ruff, S. W., Gellert, R., et al. (2010), Identification of Carbonate-Rich Outcrops on Mars by the Spirit Rover, *Science 329*, 421-424, doi:10.1126/science.1189667.

Murray, C. D. And Dermott, S. F. (1999), *Solar System Dynamics*, Cambridge Univ. Press, New York.

Neuendorf, K. K. E., Mehl, J. P., Jr., and Jackson, J. A. (eds.) (2005), *Glossary of Geology, 5th ed.*, American Geological Institute, Alexandria, Virginia.

Press, W. H., Teukolsky, S. A., Vetterling, W. T., and Flannery, B. P. (1992), *Numerical Recipes in C, 2nd ed.*, Cambridge Univ. Press, Cambridge, UK.

Qaim, S. M., Black, P. J., and Evans, M. J. (1968), The preparation of narrow-line ^{57}Fe Mössbauer sources and an investigation of some of the causes of their line broadening, *J. Phys. C (Proc. Phys. Soc), 1*, 1388, doi:10.1088/0022-3719/1/5/329.

Ramsey, M. S., and Christensen, P. R. (1998), Mineral abundance determination: Quantitative deconvolution of thermal emission spectra, *J. Geophys. Res.*, *103*(B1), 577–20, doi:10.1029/97JB02784.

Rice, J. W., Jr., Greeley, R., Li, R., et al. (2010), Geomorphology of the Columbia Hills Complex: Landslides, Volcanic Vent, and Other Home Plates, *LPSC XLI*, Abstract #2566.

Rice, M. S., Bell, J. F., III, Cloutis, E. A., et al. (2010), Silica-rich deposits and hydrated minerals at Gusev Crater, Mars: Vis-NIR spectral characterization and regional mapping, *Icarus, 205*, 375-395, doi:10.1016/j.icarus.2009.03.035.

Rieder, R., Wänke, H., Economou, T., and Turkevich, A. (1997), Determination of the chemical composition of Martian soil and rocks: The alpha proton X ray spectrometer, *J. Geophys. Res.*, *102*(E2), 4027–4044, doi:10.1029/96JE03918.

Rieder, R., Gellert, R., Brückner, J., et al. (2003), The new Athena alpha particle X-ray spectrometer for the Mars Exploration Rovers, *J. Geophys. Res.*, *108*(E12), 8066, doi:10.1029/2003JE002150.

Rover Team (1997), The Pathfinder Microrover, *J. Geophys. Res., 102*(E2), 3989–4001, doi:10.1029/96JE01922.

Ruff, S. W., Christensen, P. R., Blaney, D. L., et al. (2006), The rocks of Gusev Crater as viewed by the Mini-TES instrument, *J. Geophys. Res., 111,* E12S18, doi:10.1029/2006JE002747.

Ruff, S. W., Farmer, J. D., Calvin, W. M., et al. (2011), Characteristics, distribution, origin, and significance of opaline silica observed by the Spirit rover in Gusev crater, Mars, *J. Geophys. Res., 116,* E00F23, doi:10.1029/2010JE003767.

Ruff, S. W. and Hamilton, V. (2014), Wishstone to Watchtower: Alteration of plagioclase-rich rocks in Gusev Crater, Mars, Abstract P34A-03 presented at 2014 Fall Meeting, AGU, San Francisco, CA, 15-19 December 2014.

Schiffman, P., Zierenberg, R., Marks, N., et al. (2006). Acid-fog deposition at Kilauea volcano: A possible mechanism for the formation of siliceous-sulfate rock coatings on Mars. *Geology*, *34*(11), 921. doi:10.1130/G22620A.1.

Schmidt, M. E., Ruff, S. W., McCoy, T. J., et al. (2008), Hydrothermal origin of halogens at Home Plate, Gusev Crater, *J. Geophys. Res., 113,* E06S12, doi:10.1029/2007JE003027.

Schmidt, M. E., Farrand, W. H., Johnson, J. R., et al. (2009). Spectral, mineralogical, and geochemical variations across Home Plate, Gusev Crater, Mars indicate high and low temperature alteration. *Earth and Planet. Sc. Lett.*, *281*(3-4), 258–266, doi:10.1016/j.epsl.2009.02.030.

Smith, M. D., Wolff, M. J., Spanovich, N., et al. (2006), One Martian year of atmospheric observations using MER Mini-TES. *J. Geophys. Res.*, *111*(E12), E12S13, doi:10.1029/2006JE002770.

Squyres, S. W., Arvidson, R. E., Baumgartner, E. T., et al. (2003) Athena Mars rover science investigation, *J. Geophys. Res., 108*(E12), 8062, doi:10.1029/2003JE002121.

Squyres, S. W., Arvidson, R. E., Bell, J. F., III, et al. (2004a), The Spirit Rover's Athena Science Investigation at Gusev Crater, Mars, *Science, 305*, 794– 799, doi:10.1126/science.3050794.

Squyres, S. W., Grotzinger, J. P., Arvidson, R. E., et al. (2004b), In Situ Evidence for an Ancient Aqueous Environment at Meridiani Planum, Mars, *Science*, *306*(5702), 1709–1714. doi:10.1126/science.1104559.

Squyres, S. W., Arvidson, R. E., Blaney, D. L., et al. (2006), Rocks of the Columbia Hills, *J. Geophys. Res., 111,* E02S11, doi:10.1029/2005JE002562.

Squyres, S. W., Aharonson, O., Clark, B. C., et al. (2007), Pyroclastic activity at Home Plate in Gusev Crater, Mars, *Science, 316,* 738-742, doi: 10.1126/science.1139045.

Squyres, S. W., Arvidson, R. E., Ruff, S., et al. (2008), Detection of silica-rich deposits on Mars, *Science, 320*, 1063-1067, doi: 10.1126/science.1155429.

Squyres, S. W., Arvidson, R. E., Bell, J. F., III, et al. (2012), Ancient impact and aqueous processes at Endeavour Crater, Mars. *Science*, *336*, 570–576, doi:10.1126/science.1220476.

Stroncik, N. A., & Schmincke, H.-U. (2001). Evolution of palagonite: Crystallization, chemical changes, and element budget. *Geochemistry, Geophysics, Geosystems*, *2*(7), n/a–n/a. doi:10.1029/2000GC000102.

Tanaka, K. L. and Hartmann, W. K. (2012), The Planetary Time Scale, in *The Geologic Time Scale 2012*, *Vol. 1,* edited by F. M. Gradstein et al., pp. 275-298, Elsevier B.V., doi:10.1016/B978-0-444-59425-9.01001-5.

Thompson, A. C., Attwood, D. T., Gullikson, E. M., et al. (2001), *X-Ray Data Booklet*, edited by A. C. Thompson and D. Vaugham, *LBNL/PUB-490, Rev 2*, Lawrence Berkeley Natl. Lab., Berkeley, Calif. Available online at http://xdb.lbl.gov/.

Thompson, S., Greeley, R., Whelley, P., et al. (2004), Wind Eroded Rocks in Gusev Crater, Mars, seen from the Mars Exploration Rover, Spirit, *American Geophysical Union, Fall Meeting 2004*, abstract #P31B-0986.

Thomson, B. J., Bridges, N. T., Cohen, J., et al. (2013), Estimating rock compressive strength from Rock Abrasion Tool (RAT) grinds, *J. Geophys. Res. Planets*, *118*, 1233–1244, doi:10.1002/jgre.20061.

Tosca, N. J., McLennan, S. M., Lindsley, D. H., and Schoonen, M. A. A. (2004), Acid-sulfate weathering of synthetic Martian basalt: The acid fog model revisited. *J. Geophys. Res.*, *109*(E5), E05003. doi:10.1029/2003JE002218.

Tréguier, E., d'Uston, C., Pinet, P. C., et al. (2008). Overview of Mars surface geochemical diversity through Alpha Particle X-Ray Spectrometer data multidimensional analysis: First attempt at modeling rock alteration. *J. Geophys. Res.*, *113*(E12), E12S34, doi:10.1029/2007JE003010.

Usui, T., McSween, H. Y., Jr., and Clark, B. C., III (2008), Petrogenesis of high-phosphorous Wishstone Class rocks in Gusev Crater, Mars, *J. Geophys. Res*., *113*, E12S44, doi:10.1029/2008JE003225.

van Kan Parker, M., Zegers, T., Kneissl, T., et al. (2010), 3D Structure of the Gusev Crater Region. *EPSL, 294*, 411-423, doi:10.1016/j.epsl.2010.01.013.

Vertesi, J. (2015), *Seeing Like a Rover: How Robots, Teams, and Images Craft Knowledge of Mars*, University of Chicago Press, Chicago, Il., doi:10.7208/chicago/9780226156019.001.0001.

Wang, A., Korotev, R. L., Jolliff, B. J., et al. (2006), Evidence of phyllosilicates in Wooly Patch, an altered rock encountered at West Spur, Columbia Hills, by the Spirit rover in Gusev crater, Mars, *J. Geophys. Res., 111*, E02S16, doi:10.1029/2005JE002516.

Watters, W. A., Grotzinger, J. P., Bell, J., III, et al. (2011), Origin of the structure and planform of small impact craters in fractured targets: Endurance Crater at Meridiani Planum, Mars, *Icarus 211*, 472-497, doi:10.1016/j.icarus.2010.08.030.

Wentworth, C. K. (1922), A Scale of grade and class terms for clastic sediments. *J. Geol.*, *30*(5), 377–392. Retrieved from http://www.jstor.org/stable/30063207.

Wertheim, G. K., (1964), *Mössbauer Effect: Principles and Applications*, Academic Press, San

Diego, Calif.

Yingst, R. A., Schmidt, M. E., Herkenhoff, K. E., et al. (2007), Linking Home Plate and Algonquin Class rocks through microtextural analysis: Evidence for hydrovolcanism in the Inner Basin of Columbia Hills, Gusev Crater, *7th International Conference on Mars*, Abstract #3296.